15

Scanning Transmission Electron Microscopy and Spectroscopy of Suspended Graphene

Ursel Bangert[1], Mhairi Gass[2], Recep Zan[1] and Cheng Ta Pan[1]
[1]*The University of Manchester,*
[2]*SuperSTEM Laboratories, CCLRC Daresbury Laboratory,*
UK

1. Introduction

Transmission electron microscopy is the only technique by which freely suspended graphene can be scrutinised for nano-scale topography and chemistry occurring in micromechanically exfoliated graphene or having been introduced by production methods, e.g., by growth on Ni-subtsrates, or as a result of functionalistaion, e.g., upon hydrogenation. Investigations on this scale require atomic resolution, which can be catered for by electron microscopy; indeed several impressive studies have been conducted. In this chapter we summarise reports on scanning transmission electron microscopy and spectroscopy investigations, conducted with aberration corrected probes, especially recent results of atomic resolution high angle dark field microscopy, by which chemical information about atoms in graphene that are heavier then carbon can be obtained. By combining this with ultra-high spatially resolved electron energy loss spectroscopy to reveal the nature of elements, particularly those with lower atomic number (e.g., boron and hydrogen), which do not show up in high angle dark field images, one obtains an invaluable and powerful tool for graphene reserach; added to this is the information about the electronic bandstructure that can be obtained on a highly spatially resolved scale through monitoring the plasmon behaviour of graphene.

Paragraph 2 briefly describes the scanning transmission electron microscopy (STEM) technique employed for imaging and chemical analysis, and how free-standing membranes of graphene, required for these measurements, are obtained. Paragraph 3 deals with high resolution imaging of the atomic structure and configuration of intrinsic defects and paragraph 4 with stabilisation issues of single and bi-layer membranes: rippling effects in the graphene lattice are revealed. In free-standing CVD-grown graphene the membranes are an intricate patchwork of mono- and bi-layers, the latter being AB stacked or rotated at various angles to each other. In paragraph 5 atomic resolution HAADF and ultra-high spatially resolved electron energy loss spectroscopy are used to identify atomic sites and chemical nature of metal impurity atoms Au, Ni and Fe, as well as of B, intentionally introduced into graphene as electronic dopant via ion implantation. It is highly desirable to be able to reveal the presence and distribution of hydrogen in order to assess the success of H-dosing for the purpose of bandgap tailoring; we investigate the applicability of energy loss spectrum imaging for this purpose. Paragraph 6 scrutinises plasmon characteristics of graphene. Plasmon behaviour is sensitive to electron densities and electronic structure of

solids; the graphitic σ-plasmon undergoes typical changes in few-layer structures and provides an unambiguous fingerprint for single layer graphene, whilst the graphitic π-plasmon can give valuable information about changes in the π-electron system upon doping and dosing. In combination with DFT calculations we test the scope of plasmon spectroscopy in assessing, especially, H-induced graphene morphologies.

2. Microscopy methods and TEM sample preparation techniques

2.1 Microscopy methods

Electron microscopy studies of graphene so far have been conducted in a transmission electron microscope (TEM), using a stationary electron beam. Here we use an aberration corrected (AC) transmission electron microscope (STEM) (Goodhew & Bleloch, 2003) with a cold field emission gun and added, analytical facilities. In a STEM a focussed electron probe is scanned in a pixelated raster over a pre-defined sample area. The benefits of this microscope are the very bright (100 pA) and very fine (≤0.1 nm diameter) probe, which, due to the small depth of focus (8nm) provides an image- (pixel-) resolution of better then 0.1 nm, allowing atomic-scale imaging to be carried out in bright field (BF) and, very importantly, in high angle annular dark field (HAADF) mode. A further benefit is the variable operating voltage from 100 down to 60 kV, ensuring measurements below the displacement threshold of C (at ~80 keV).

In BF mode electrons from the central diffraction disk are collected over an angular range of 0-6 mrad. Diffraction disks (rather then spots) are formed because of the high beam convergence angle (~24 mrad). The occurrence of atomic lattice images at high resolution arises from coherence (phase) effects in overlapping diffraction disks. In HAADF mode electrons scattered to high angles are collected in an annular detector with an angular range of 70-210 mrad. These electrons have undergone incoherent elastic scattering (Rutherford scattering), the strength (or probability) of which is approximately proportional to the square of the atomic number of the scattering element (Z-contrast), and therefore this imaging method can be used for chemical identification (Pennycook & Boatner, 1988). At high magnifications, due to the fine probe and employing sub-Å scan point separation, individual atoms can be 'lined-out', giving rise to atomic resolution HAADF images. Such images can be interpreted rather straight forwardly and much more easily than BF phase contrast images.

Chemical/elemental analysis using electron energy loss spectroscopy (EELS) (Brydson, 2003; Egerton, 1986) can be conducted with high sensitivity at the same spatial resolution as obtained in images. Inelastic scattering events can be detected with collection angles of up to 19 mrad over an energy range of 0-2000 eV, covering energy losses from valence band to K-shell core loss excitations of elements spanning the periodic table from H to noble metals (using an 'Enfina' energy loss spectrometer). The combination of the ~0.3 eV energy resolution and energy dispersions of up to 0.01 eV/channel provides access to absorption events in the 1 eV loss regime, thus enabling electronic bandstructure studies. Energy loss spectra can be obtained as individual spectra in single locations on the sample or as collective data sets along predefined lines (line scans) or in predefined image areas (spectrum images (Hunt & Williams, 1991)). The small probe size enables EELS to be carried out even on single atoms (Browning & Pennycook 1994). Image acquisition and processing as well as EELS measurements and evaluation were conducted with the Gatan Digital Micrograph software and its various 'plug-ins'; data analysis using special programs is described in the respective paragraphs.

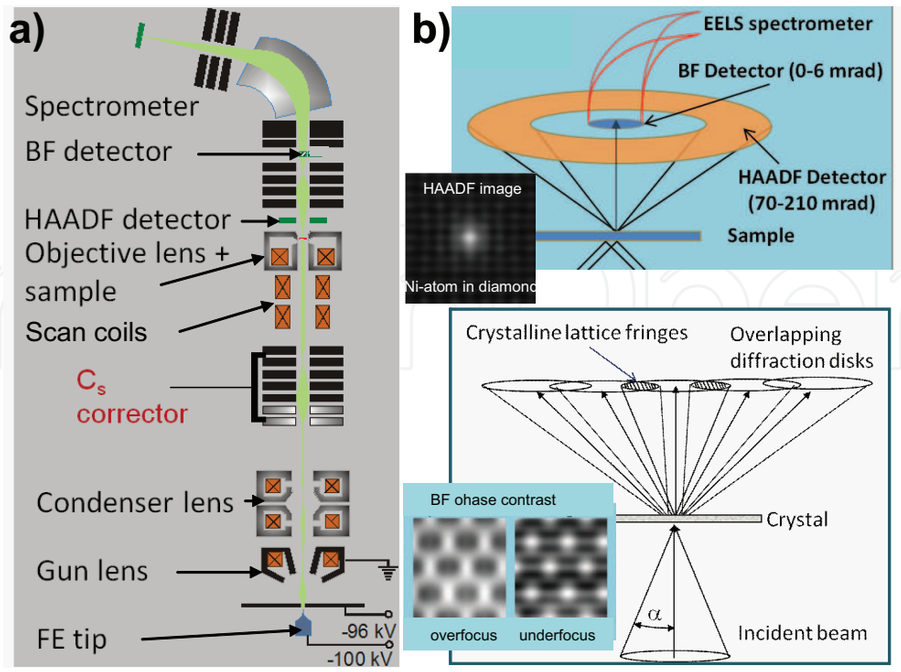

Fig. 1. a) Schematics of the STEM, b) enlarged detail of detector configuration with schematic HAADF image inset (top panel) and schematics of origin of phase contrast on the BF detector with inset showing lattice images in overfocus and underfocus (bottom panel).

The Daresbury SuperSTEMs (the UK's first aberration corrected STEMs) were used for STEM imaging and analysis. TEM results, which are also presented in this chapter, were obtained with a Tecnai F30.

2.2 TEM sample preparation

There are several methods to acquire suspended graphene layers, initially such layers were obtained by micro-mechanical cleaving and exfoliation (Booth et al, 2008). After repeated cleaving of graphite by using adhesive tape, thin flakes are transferred to an oxidised Si wafer on which few-layer graphene flakes can be identified by their colour using a light microscope. Selected flakes are then made to adhere to a TEM sample grid; this is facilitated by using, e.g., sticky grids (Quantifoil), and employing the surface tension of a drop of evaporating IPA, dripped onto the graphene flakes.

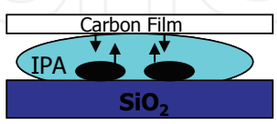

Another frequently used method employs embedding of graphene flakes in PMMA or CAB (Cellulose Acetate Butyrate) for protection, and subsequent lift off the substrate (e.g., by etching the substrate), and floating the PMMA (or CBA) containing the graphene flakes off. The details of this procedure can vary; the steps outlined in the sketch below entail for example applying a sticky tape (blue) with a window (step 2) to make a 'frame' for easier handling of the PMMA/graphene film during the transfer to the TEM grid. This sticky tape is later removed by scribing the PMMA around the target area (step 5)

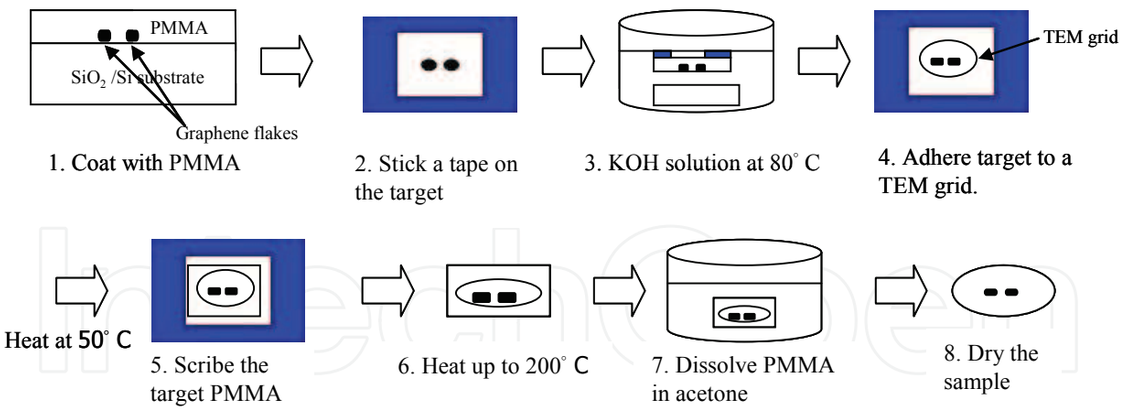

Figure 2a) shows an optical micrograph of graphene flakes obtained by micromechanical cleaving and deposition across a crack (induced by cleaving) in an oxidised Si wafer. The darkish blue graphene areas are identified as single or bi-layers. The graphene is freely suspended, where it lies across the gap and hence could be directly imaged in a TEM using the Si as sample support. Figures 2b-d are TEM BF images of the suspended flake at increasing magnification. Figure 2c shows that the graphene surface has significant contamination; 2d) shows the atomic lattice in an uncontaminated patch. Figure 2e) is a HAADF STEM image at low magnification with contamination, most likely hydrocarbon deposits, presenting them selves as whitish contrast. These deposits are interrupted by dark patches, representing uncontaminated parts of single layers. In the following paragraph it is the atomic scale topography of uncontaminated patches that we will concern ourselves with. Figures 2e&f are views at increased magnification. Figure 2g), although noisy, as it represents scattering of one single atomic layer, shows the graphene lattice. Much of the work in the following paragraphs will focus on HAADF studies, which we have carried out in the SuperSTEM; a number of papers have dealt with transmission electron microscopy (TEM) of graphene (Meyer et. al., 2007a; Meyer et. al., 2008a; Meyer et. al., 2008b) however HAADF studies have not been amongst these.

3. Atomic scale topography: defects and ad-atoms

3.1 Defects

In the case of graphene with the electron beam focussed onto the sheet, the rare occasions occurs, where electron microscopy lattice images can be seen as a direct depiction of the ball-and-stick model of an atomic lattice structure. These images are directly interpretable: bright contrast corresponds to atoms and dark contrast to the gaps in between. Effects of atomic structure extending in direction of the electron beam, resulting in de-channelling of the beam on atomic columns and hence inducing contrast changes etc, cannot occur in mono-layer structures. Moreover, the atomic arrangements of atomic-scale defects can be straight forwardly deduced. HAADF can furthermore reveal the atomic nature of species at single-atom level through the approximate Z^2-dependence of the scattering probability. It is thus feasible for detection of atom species on/in graphene of Z equal to and larger then carbon. Graphene has provided the basis for elegant theoretical calculations and predictions of defect structures alongside their effects on the physical, chemical and electronic properties (Duplock, Scheffer & Lindan, 2004; Crespi, Scheffler & Rubio, 1997; Charlier, 2002). Structural observations on suspended graphene, on the other hand, are still relatively scarce, and, as

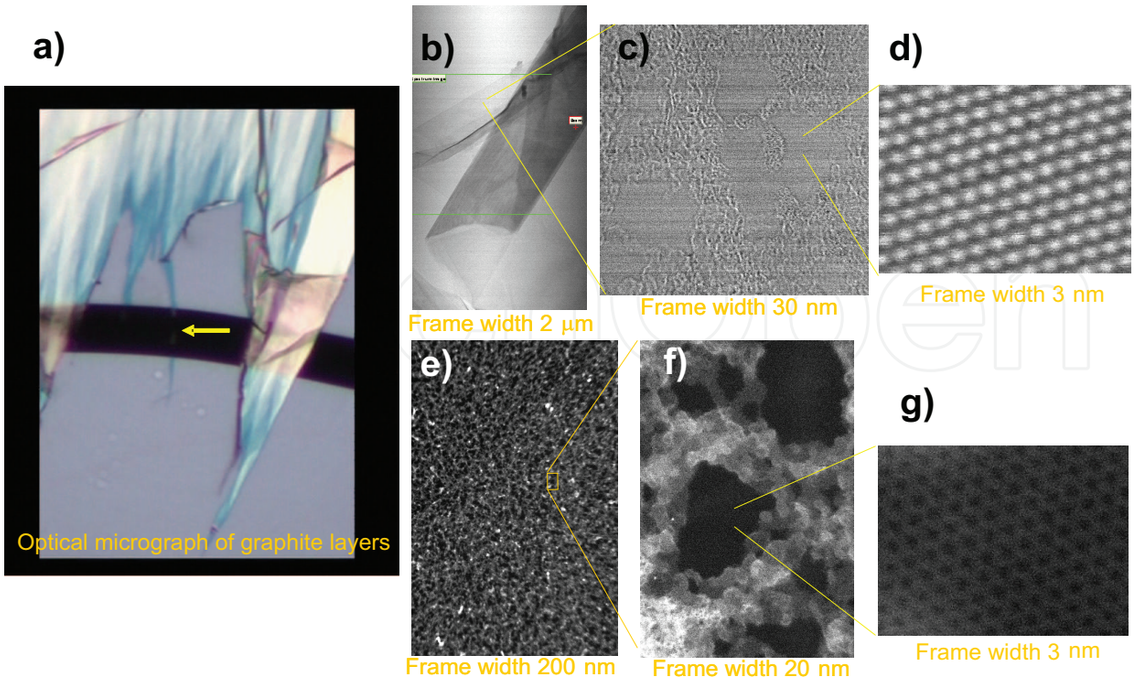

Fig. 2. a) optical micrograph of graphene flake deposited across a gap in an oxidised Si-wafer, b), c) and d) BF TEM images and e), f) and g) HAADF STEM images of the flake at increasing magnification.

noted earlier, HAADF studies are non-existent. Here we reveal directly atomic scale topological features of free standing graphene.

Electron beam energies of 100 keV, used for some of the following studies are just around the displacement threshold for atoms in carbon structures. Hence it is difficult to judge, whether defects occurring during the first image scan are radiation induced, or whether they were already present. However, changes in the films occurring over multiple scans were carefully monitored (and captured in movies), and on the basis of this it appears that discernible changes took place only after ~2 minutes of repeated scanning, and that the defect numbers during the first few scans are very small and stay constant, with the defects well separated (although some movement / reconstruction was observed even between initial scans). It is of interest to follow in-situ defect formation in the STEM, captured in sequential scans, each scan lasting no longer then 10 s. Figure 3 shows the 1st, 17th, 18th and 19th image of a 20-images series of STEM high resolution BF images. Only in the later scans, after ~2 min irradiation, does e-beam defect formation become a distinctive feature. At that stage a large number of single point defects- seen here are vacancies- suddenly appears (fig. 3c, red circle). These aggregate to form larger clusters (fig. 3d, red circle) and, eventually, holes. We emphasise we are dealing with BF-phase contrast images; these are not as directly interpretable as their HAADF counterparts. Nevertheless, since the images here were taken at ~1nm overfocus, the centre of the 6-rings, and also vacancies, will appear darker then the atoms, similar to dark field images. The delay in the apparent setoff of the beam damage may indicate that a small number of defects are already present in graphene sheets, and almost all of these are single vacancies. However, this contradicts STM studies of graphene obtained by micro-cleavage, in which the authors were unable to detect one single vacancy

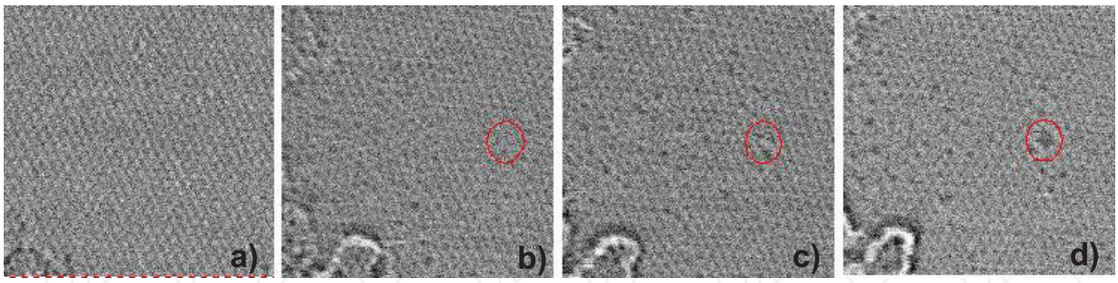

Fig. 3. Snapshots of a BF image series demonstrating development of radiation induced defects in the STEM. The darks spots are vacancy related defects. a) frame 1, b) frame 17 c) frame 18, d) frame 19; the scan time per frame was ~10 s.

(Stolyarova, 2007). Alternatively, the electron beam can radicalize molecules absorbed on the surface, which react with carbon leading to broken bonds.

Figure 4a) depicts a single-layer area imaged in HAADF. Although the lattice is visible in the raw HAADF images, it is feasible to reduce the noise by applying either a deconvolution routine based on maximum entropy image reconstruction (HREM Research Inc., 2009) or a low pass Fourier filtering method. The former sharpens features by deconvolving the images with a simulated electron probe function having a Gaussian or Lorentzian profile (or a combination of both), thus constituting a software C_s corrector, the latter improves visibility of spatial frequencies by applying a mask to the Fourier transformed (FFT) image, which includes the spatial frequencies right up to the lowest order *a*-plane diffraction spots, as well as the *a*-plane ([100], [010] and [-110]) reflections themselves (inset top left), and then obtaining the inverse Fourier transform (IFFT).

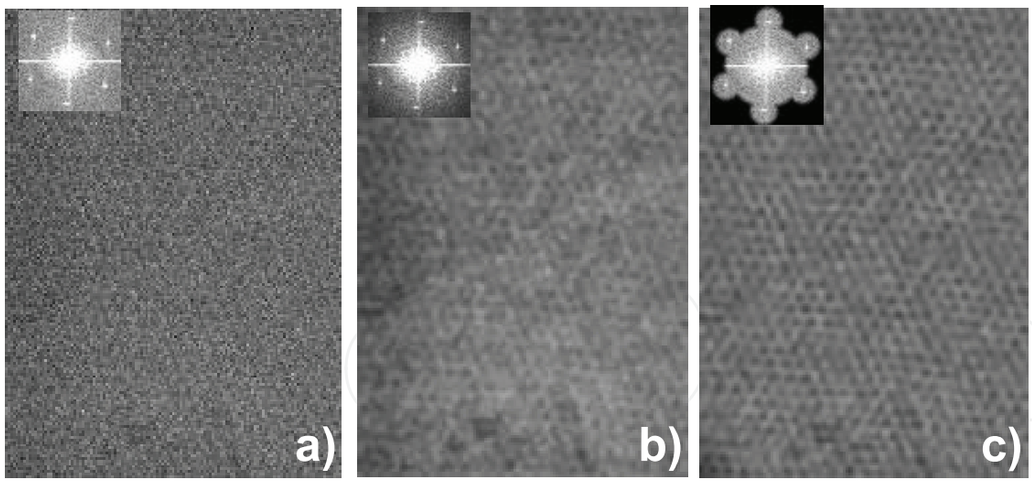

Fig. 4. a) raw HAADF image of single graphene sheet with FFT as inset, b) same HAADF image after deconvolution; the FFT in the inset is clearer as a result of noise reduction, c) IFFT of area in (a) having applied the band pass filter in the inset.

Noise reduction using deconvolution is shown in fig.4b. The low pass filter (fig.4c) achieves noise reduction by cutting out high frequencies; it preserves the information of all direct space distances larger then the a-lattice plane spacing and additionally superimposes a 'directional' component as frequencies between diffraction spots are masked out, thus enhancing the graphene lattice. In the following this latter filter is used. In order to

investigate possible artefacts introduced into the IFFT, i.e., into the end image, by the mask edges and the background noise, we subtracted a filtered Fourier transformed vacuum image from the filtered graphene Fourier space image, before we applied the inverse transform. However, this showed insignificant change in the case of this particular filter.
The vast majority of defects are vacancies. The HAADF lattice images in figures 5a and 5b are filtered in the described fashion, showing enlarged lattice structure surrounding a mono- and a di-vacancy with overlaid model structure (Gass et al., 2008). These are easy to discern, whereas Stone-Wales defects (Terrones & Terrones, 1996), constituting a reconfigured, rotated bond have not been identified so far.

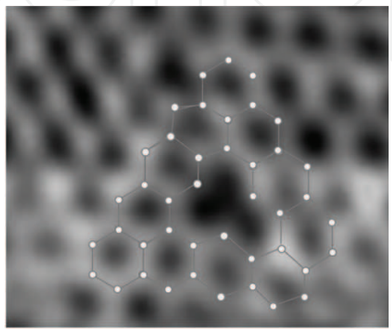

(a)

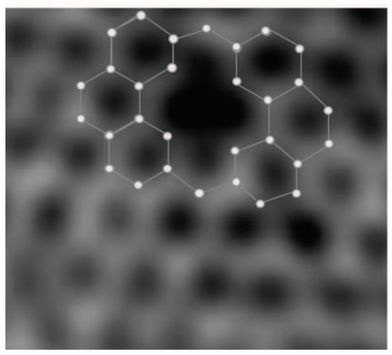

(b)

Fig. 5. a) and b): enlarged areas in HAADF images after low pass filtering showing a single vacancy and a di-vacancy with overlaid ball and stick models

There is a wealth of literature dealing with defects in HPO graphite [e.g. Hahn & Kang, 1999; Bourelle, Konno & Inagaki, 1999, Telling & Heggie 2007; Krasheninnikov et. al. 2001]. Isolated point defects on the surface of graphite are exlusively reported in connection with irradiation damage or ion bombardment, this might indicate that even the defects seen in the very first scan occur due to electron bombardment.
However, we also observe a second type of defect, related to the termination of a row of hexagons, and hence representing the 2-D or mono-layer equivalent of a dislocation (Gass et al., 2008). There are two species of unit c-axis edge dislocation in graphitic materials [Jenkins, 1969], depending on whether their glide plane cuts between atoms closely spaced in this direction or between atoms separated by a full bond length (defined as 'shuffle' and 'glide' plane respectively [Ewels, 2002]). After bond reconstruction, these two dislocation cores consist of either a pentagon-heptagon pair (5-7 defect, 'glide plane' dislocation core),

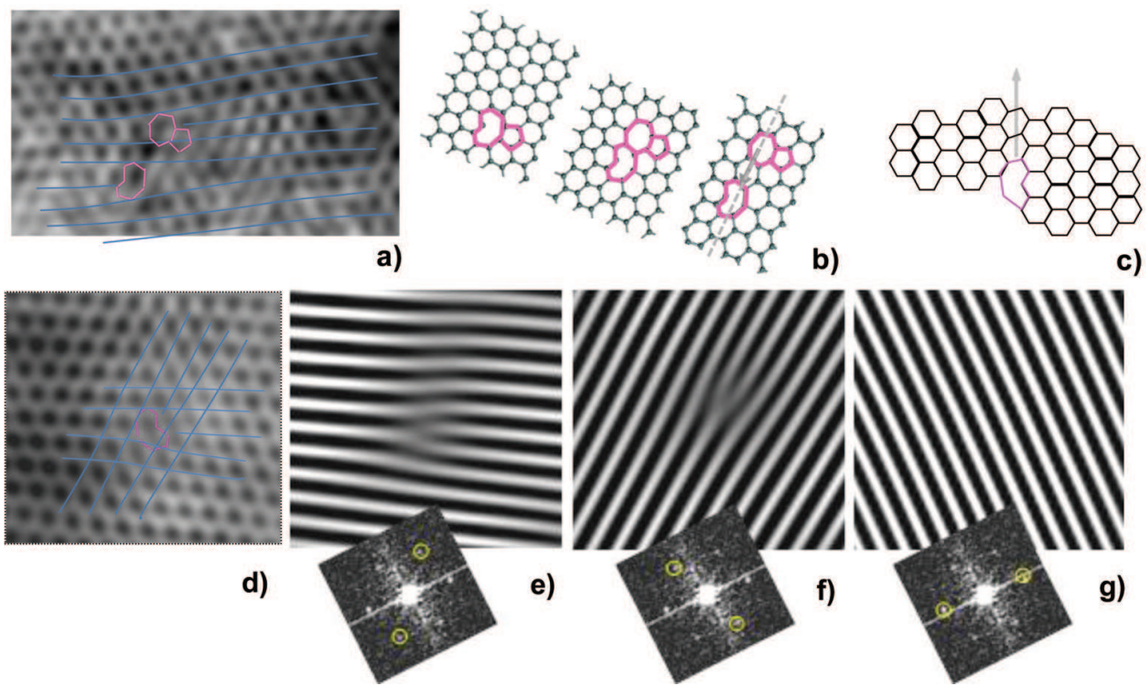

Fig. 6. a) HAADF image of dissociated shuffle-glide dipole (purple) with lattice 'planes' indicated in blue, b) model of an undissociated dipole (purple), formed by only one vacancy (leftmost panel), and subsequent separation into glide and shuffle defect via glide of the shuffle segment along the plane indicated by the dashed grey line (rightmost panel), c) formation of a shuffle defect by bond reconstruction at the edge of a graphene sheet; glide inwards along the grey arrow might be achieved by shear stress, leading as in (b) to the termination of a row of atoms, d) HAADF image of a single defect, which could have formed according to (c), e), f) and g) IFFTs obtained by masking the respective diffraction spots in the FFTs of (d), revealing termination of two different rows of atoms at the defect.

or a pentagon-heptagon pair with a 2-fold coordinated ad-atom carbon in the central bond ('shuffle' plane dislocation core; see figure 6b, e.g., 3rd schematic). These two dislocations were shown to migrate with radically different activation barriers, namely, 7.64eV for the glide core, 2.22eV for the shuffle core [Ewels, 2002]. This difference was explained in terms of the mechanism of motion. Motion occurs through a 90° rotation of a C-C bond along one side of the heptagon. For the glide dislocation core this requires breaking two C-C bonds, whereas in the shuffle dislocation core the same effect can be achieved through breaking and formation of just one bond. Thus the additional atom at the core of the shuffle dislocation is able to catalyse the motion of the dislocation [Ewels, 2002]. The glide dislocation core is essentially immobile. A single vacancy can be considered a dislocation dipole, with the two dislocations of opposite sign facing each other on neighbouring glide planes, as shown in fig. 6b (1st schematic). The 2nd and 3rd schematic in fig. 6b show dissociation of the dipole along the glide plane. The 3rd schematic depicts indeed the situation in the HAADF image of such a dissociated shuffle-glide dipole in fig. 6a.

Another possible route to create a shuffle core is through reconstruction of the edge of a graphene layer, which exhibits a distortion, as shown in fig. 6c (see row of sheared hexagons). Here an 8-atom ring defect bridges a corner. Under shear stress along the grey arrow, the defect could glide into the layer. This requires neither formation of a dipole nor vacancies, and each glide step, i.e., moving the defect by one hexagon along the grey line, only requires reconstruction of one bond. The HAADF image in figure 6d shows a single shuffle dislocation core with a clearly visible under-coordinated carbon atom in the defect core. We have demonstrated in fig. 3 that vacancies move easily under electron beam irradiation, so the e-beam facilitates glide. The presence of residual stresses (e.g., originating from micromechanical cleaving and exfoliation of the graphene) might be an additional source for glide of 8-atom ring defects formed at graphene edges.

3.2 Adatoms

Lattice resolution HAADF images of uncontaminated patches in single layer graphene films show contrast variations in the benzene rings. This can be observed in the previous figures. The area in figure 7a) is part of a clean patch and has been Fourier filtered, using a low pass filter (like this in figure 4). It becomes clear that the graphene lattice is not of uniform contrast; some of the bridges between atoms are significantly brighter. The ball and stick model, overlaid in the top right indicates the bright regions as ad-atoms. To the left of the overlaid model there is a vacancy (marked 'V'). We suggest that the regions of enhanced brightness found in fair numbers are due to C-adatoms, forming bridges above the in-plane C-C bonds. We derive this from a quantitative evaluation of the HAADF contrast (Bangert et al., 2009b). Examples of the quantification are shown in fig 7b, which includes intensity profiles (blue curves) that had been taken in *raw*, i.e., unfiltered HAADF images; the scan lines are marked in 7a) to indicate the corresponding scan locations in the filtered image. The red curves in the two panels are intensity scans across a vacuum image. They show the counts arising from camera shot noise and electron background when the beam is not on the specimen. The base line in the graphene is higher then in the vacuum image due to scattering from a single atomic layer; the high frequency variations in the intensity in the curves are of statistical nature, but it has to be noted that a lower frequency pattern with troughs and peaks modulates the noise around the base line intensity in the blue curves; this pattern reflects the periodicity of the atom array, as the 1-Å probe causes higher intensities on then between atoms. Distinctively above the graphene layer intensity are 'spikes' (orange arrows) of just below twice the intensity. These correlate with positions of the brighter 'bridges', indicated by corresponding orange arrows in the low pass filtered image. The HAADF contrast scales near linearly with the material thickness, i.e., with the number of atomic layers traversed by the e-beam. It scales, however, approximately with the square of the atomic number: measured ratios of HAADF signals from C-atoms in graphene and single atoms of Si or Cu contaminants, the nature of which was confirmed by EELS, revealed a power dependence of slightly less then 2. The HAADF intensity on the ad-atoms increases by a factor of just less then 2, whereas it should increase by 2½ or 3 times if these atoms were N or O; such an increase would lie outside the statistical error interval. In addition, highly localised core loss spectra (not shown) encompassing the range from C to O showed no sign of N and O.

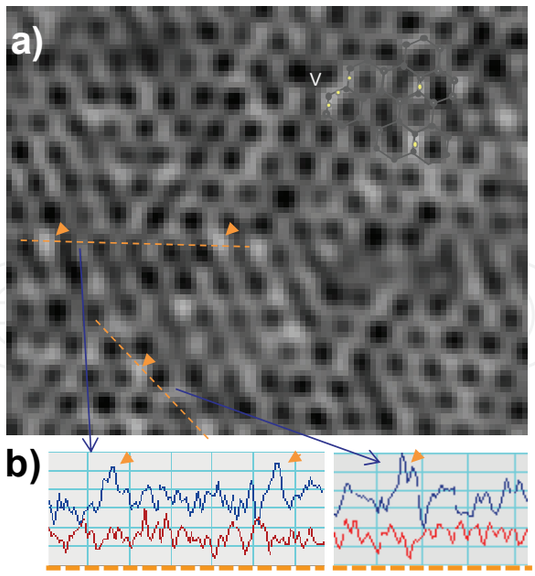

Fig. 7. a) Enlarged region from the filtered HAADF image in figure 4c with ball-and-stick model overlaid in the top right corner and a vacancy V indicated. Shown also are lines along which the intensity profiles displayed in b), blue curves, were taken. Intensity line-profiles from vacuum images are in red. Spikes of ~2x the graphene intensity are indicated with orange arrows. Enhanced intensity in the corresponding locations is emphasised and arrowed in (a). All intensity profiles were taken on raw, unprocessed images.

Carbon ad-atoms on graphene have previously been suggested (Meyer et. al. 2008b; Nordlund, Keinonen & Mattila, 1996). However, from HAADF contrast it cannot be excluded that H-atoms, too, are bound to C-adatoms or, indeed, directly to graphene C-atoms. Their Z-contrast would be lost in the noise.

4. Nano-scale topography: ripples in monolayers and turbostratic arrangements in bi-layers

4.1 Ripples

The stability of extended two-dimensional (2D) structures has been the subject of a long-standing theoretical debate, with previous suggestions that 2D films embedded in three-dimensional 3D space are crinkled. It was then countered that crinkles can be suppressed by anharmonic coupling between bending and stretching modes, such that a 2D membrane can exist but will nevertheless exhibit height fluctuations (Nelson, Piran & Weinberg, 2004; Gass et. al. 2008; Meyer et. al. 2007a&b;). The mechanical behavior of graphene can have profound impact on its extraordinary electronic properties. Recent observations suggest that suspended graphene is not perfectly flat, but rather exhibits microscopic corrugations (ripples) which can be not only dynamic (that is, through flexural phonons) but also static (Gass et. al., 2008; Booth et. al. 2008; Meyer et. al. 2007b). In those observations, large-scale ripples (>15 nm) were visualized directly (Nordlund, Keinonen & Mattila, 1996) whereas ripples on a nanoscopic scale (<15 nm) were only identified from the broadening of diffraction spots (Meyer et. al., 2007b) which prevents static bending from being distinguished from dynamic bending. Furthermore, it was argued that scaffolds supporting

graphene crystals and contamination by adsorbed hydrocarbons, can induce an external compression resulting in ripples especially on the large scale, or films remember the initial non-flat configuration induced by a silicon oxide substrate used for sample preparation. In either instance, the observed ripples would not be intrinsic. The difficulty with directly imaging ripples in a transmission electron microscope arises from their small amplitude: the defocus, even with aberration-correction, is not precise enough to reliably detail changes in contrast which would arise from height differences less than a few nanometers, let alone one nanometer.

Observing perpendicularly onto an undulating plane of atoms, the bond inclination will cause variations in the projected bondlength. For example, inclinations of ~5° from the horizontal flat sheet will give rise to a change in the projected C-C bond lengths of ~1 %. Ripples possessing a wavelength of 5 nm, thus have an amplitude of 0.25 nm (this value being derived from electron beam diffraction (Meyer et al., 2007a)). However, such bond length changes are not easily observed in raw or even low-pass filtered HAADF lattice images, as seen using the filter detailed in fig. 4b and c. As FFTs of nano-scale areas, like in our case, are embedded in significant noise, the error in positioning the diffraction spot maxima gives rise to a bond length error of ~±2% in BF images, and slightly less in HAADF images. Applying a narrow annular band pass filter, with a band width corresponding to ~0.04 Å, i.e., imposing a narrow ring mask on the Fourier transform (FFT) of the raw images, passes spatial frequencies within ~2% of a selected frequency corresponding to a real space distance. The inverse transform (IFFT) reveals locations of atoms with such spacings, although with possible rotations, through intense lattice fringes. For graphene, the color coding is selected such that atoms possessing the correct bond length appear orange. Should the projected bond length change by as little as 2% owing to out-of plane bending of the atoms, the lattice periodicity will become less visible in the IFFT, and blurred patches will occur at such locations. Such regions appear blue. An example of this procedure shows ring filter and the resultant IFFT, respectively, in fig. 8a) and 8b). The latter is the projected bond length visualization; atomic scale detail can be seen as a fine raster superimposed on the colors. To better reveal the sheet rippling effect, the atomic detail has been removed by a Gaussian blurring function in the image in fig. 8d). In the Gaussian filtered images again, orange (blue) regions correspond to areas of small (large) deviations from the graphitic ***a***-plane distance of pristine and perfectly flat graphene sheets. Any spatial frequencies outside an annular mask diameter corresponding to the graphitic ***a***-plane spacing, will possess significantly weaker intensity; the color-coded IFFT resulting from both, a smaller or larger band pass would therefore be expected to exhibit more bluish colors. Since flanks of undulations reduce the projected bond length, they become visible as bluish regions in IFFTs obtained with a narrow ring mask.

We have obtained IFFTs of a number graphene images, using a series of filter diameters in each case, with increments corresponding to 0.02 Å (such an increment would arise from an inclination of ~5°), and with the above bandwidth of 0.04 Å. Although the ring mask increment lies within the error of measurement, it is still possible to follow gradual changes in contrast. In such a series of IFFT images, the spacing range covers ±10% variation of the graphitic ***a***-plane distance. In each IFFT image, a different projected lattice spacing is passed by the respective filter and comes 'into focus'; this is equivalent to observing the lattice in slices 'cut' through the crumpled 3D graphene sheet at different distances parallel to the flat sheet reference plane. In figure 9a and b, selected images from a series of IFFTs using ring mask diameter increments as described are detailed, the masks were applied to raw, single

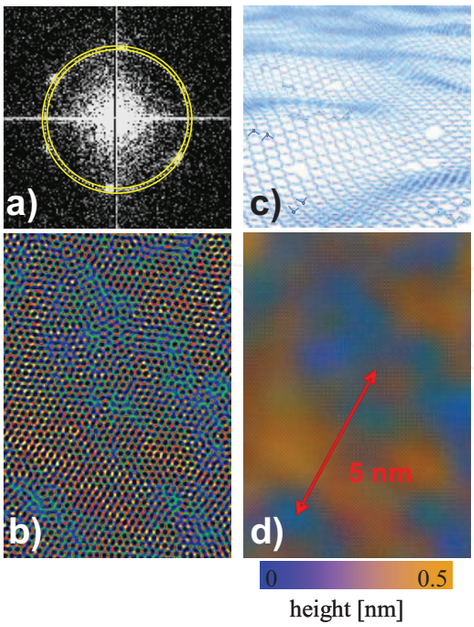

Fig. 8. a) A ring mask typically used to construct the IFFTs in (b), which is the inverse FFT of a raw HAADF image. c) Model of graphene, with undulations and defects. d) Gaussian-blurred image of (b) with the atomic detail removed, to highlight larger scale structure (flanks of undulations appear blue, approximate height scale given underneath in colour with flank inflection points set at zero).

layer images, i.e. allowing spatial frequencies both below and above the first order diffraction spot distance to pass. Fig. 9 (uppermost and middle rows) detail identical features imaged in BF and HAADF, with their associated IFFTs. BF IFFTs for the same band pass are very similar in their overall pattern to those of HAADF images, taking into account that the color scheme is slightly different in both cases. This lends credibility to the method being applied to HAADF images with weak intensities. The strongest intensity variations (orange to blue) can be observed in Fig. 9 columns iv-vii, where the ***a***-plane frequency has filtered through, whilst deviations from this band pass result in images of overall lower contrast (bluish colors, columns ii, iii and viii). In row c, the same method is applied to a 5-layer graphene sample, (the number of graphene layers was determined using the procedures described in chapter 6 and also in (Eberlein et. al., 2008). The breadth of images exhibiting the brown-orange colors (columns iv-vii) suggests flatter sheets, but also reflects the accuracy limit of the measurement; however, the radius of the ring filter used in column v (blue arrow) corresponds most closely to the ***a***-plane spacing. We note that pattern changes with band passes larger than the graphitic *a*-plane frequency (right of arrow, i.e. in columns vi and vii.) arise from a reduction in the bond length projection. For example, the circled locations mark contrast inversions, where the lattice at the flank of a ripple comes into focus, and then goes out of focus. In a simplistic picture, the peaks / troughs of ripples should be 'in focus' at the same band pass as the flat sheet, and the flanks should then be 'out of focus'. The increment in the annular filter radius required to change the color from brown to blue (images in rows a and b, columns vi and vii, circled area), allows one to deduce the inclination angle as ~12°. The ripple width of ~5 nm yields a height of ~0.5 nm. Although this is slightly greater than the value reported (Meyer et. al., 2007b; Fasolino, Los

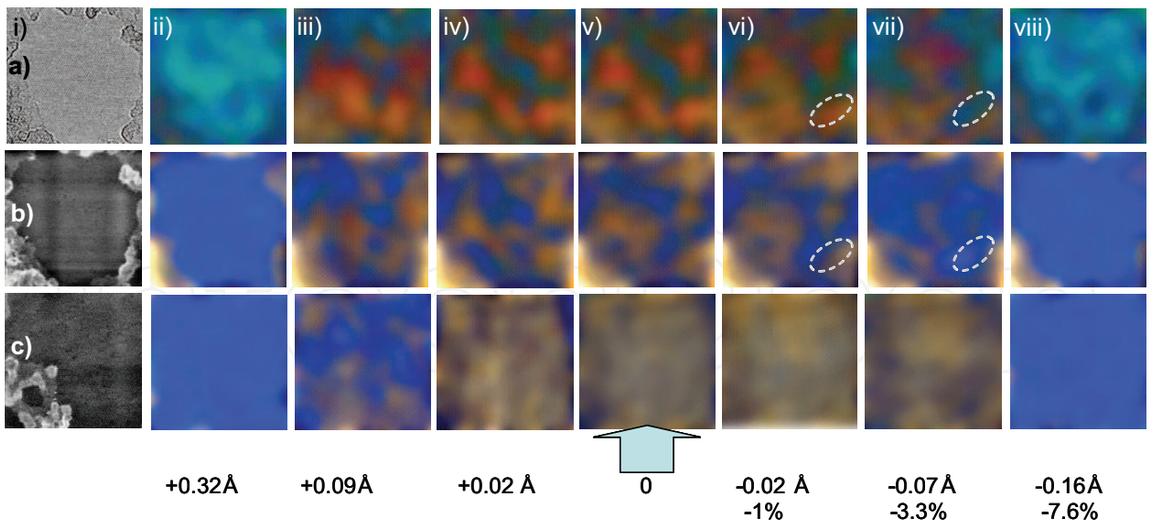

Fig. 9. In a) image (i) is a BF lattice image of a clean patch in a single graphene sheet, from which the IFFTs in (ii) to (viii) are obtained. All IFFT images have undergone Gaussian blurring. The arrow in column (v) marks the image corresponding to the correct graphitic lattice spacing. Bandpass deviations from the graphitic ***a***-plane spacing, and hence from the C-C bond length are, (ii) +15%, (iii) +4.3%, (iv) +1%, (v) none, (vi) -1%, (vii) -3.3% and (viii) -7.6%. In b) (i) represents the HAADF lattice image of the same area as in (a), and in c) (i) is the HAADF image of a 5-layer graphene patch. (ii) to (viii) in (b) and (c) represent IFFTs of the respective images in (i) with the same band pass filters as detailed for (a) above. The frame width of panels is 15 nm.

& Katnelson, 2007), ripples of this height are frequent in occurrence and pronounced in our samples. Ripples of lesser height are most likely present too, but they are concealed by larger undulations and are also close to the resolution limit of the present method: the smallest increment in Fig. 9 corresponds to 1% change in spatial frequency equivalent to ~6° inclination. The contrast variations reflect the complex and intricate sheet buckling, which is quite severe in certain regions. Additionally, topography on a larger scale arising from thin hydrocarbon deposits, as can be seen bordering 'clean' areas' in all lower magnification images of graphene, also affects the IFFT image: such deposits introduce some amorphicity, hence many spatial frequencies are present in such locations, ranging from the lattice frequency down to low frequencies representing local, large scale disturbances. This accounts for the pink coloration occurring at such locations at all band passes.
Although undulations are observed in every clean graphene 'patch' (graphene area free from hydro-carbon deposit that is) in the absence of visible topological defects, we observe that the ripple patterns can, however, be influenced by the latter. Further results on this are given in Bangert et al. (2009a).

4.2 Turbostratic graphene

All results shown so far were obtained of micro-mechanically cleaved and exfoliated graphene. Electron microscopy investigations were also carried out on graphene grown by chemical vapour deposition (CVD) on nickel and copper substrates and lifted off these substrates via aforementioned procedures. We note that hydrocarbon contamination is generally more extensive and more finely dispersed on all such samples.

The images in figure 10, in contrast to the STEM images of the previous figures, are high resolution phase contrast images, obtained in a transmission electron microscope, a Tecnai F30. Ni-grown samples consisted of large films (10's to 100's of μm), partially consisting of single layer, but in the main of few-and bi-layers, either in graphitic AB stacking or in turbostratic arrangements (de-coupled layers, rotated at various angles with respect to each other). Figure 10a) depicts suspended CVD-graphene extracted from a Ni substrate. The small omni-present worm-like contrast arises from molecular hydrocarbons, presumably in form of chains, on the surface of bi- or triple-layer graphene. This contrast is present on all such CVD sample surfaces, uncontaminated surface areas are only of the order of few nm; upon closer inspection (fig. 10a might have to be viewed with slight enlargement) the underlying graphene lattice becomes obvious. The inset in the left hand top corner is an electron diffraction pattern of the image area, revealing the turbostratic nature by the two hexagonal spot patterns rotated with respect to each other (12 spots instead of 6). The right hand bottom inset is the FFT of the image, showing the same orientation relationship of the sheets as the diffraction pattern. Areas with apparent AB stacking can also be found (not shown here). This might, however, arise from differences in the rotation angle across the film: fig 10c) shows a schematics of graphene sheet rotated with respect to each other with different rotation angles, leading to varying Moiré patterns and different atomic lattice appearances within.

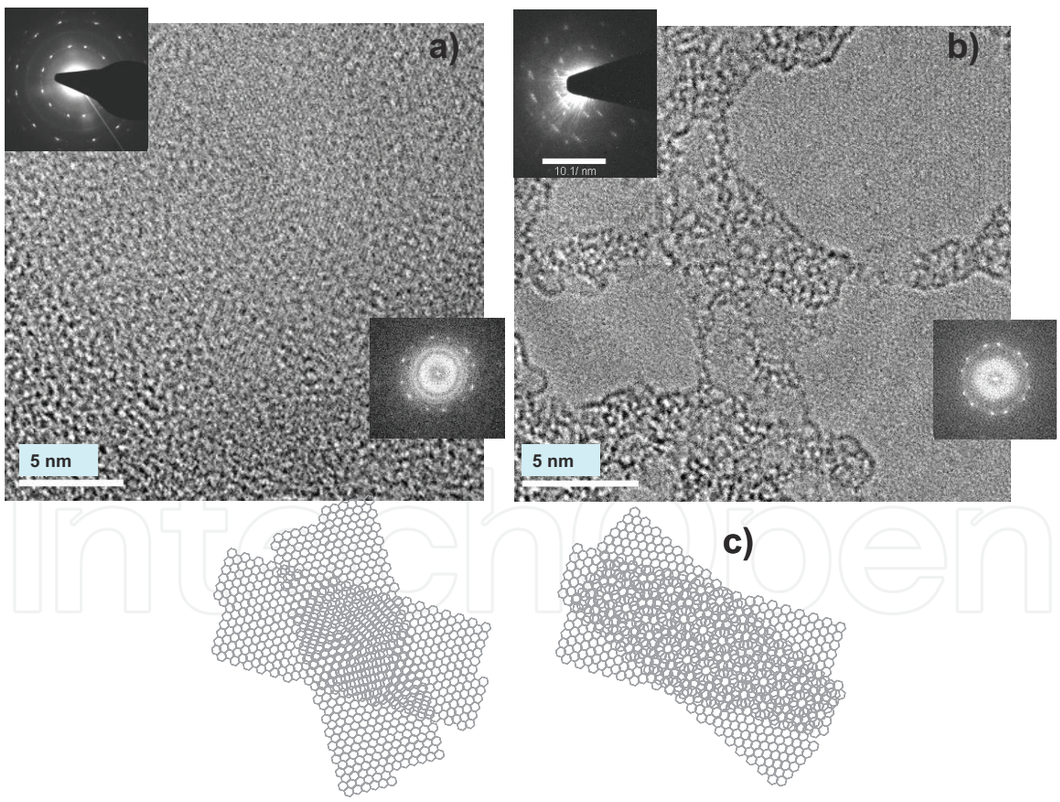

Fig. 10. HREM phase contrast images of suspended graphene grown by CVD after lift-off from a) a nickel and b) a copper substrate. Insets in both cases are the experimental diffraction pattern (top left in each image) and the Fast Fourier Transform (FFT; bottom right) of the image areas shown; c) schematics of turbostratic arrangements leading to different appearances of the atomic-scale structure.

Figure 10b) shows an image of suspended CVD-graphene grown on copper. Regions of larger uncontaminated areas (some 10s of nm) are found in these samples, however, the films consist in large, like in the Ni-substrate case, of turbostratic graphene. The insets show again the electron diffraction pattern (left top) and the FFT (right bottom) of the image area. Close inspection of the lattice structure reveals a Moiré pattern similar to the right-hand schematics in fig.10c).
Hence micromechanically exfoliated and CVD-grown graphene have quite different topographies, larger single-layer areas appear to be rare in the latter.

5. Atomic scale chemical information: impurities- native, dosed and doped

5.1 Impurities with Z ≥ 6

We have explained and demonstrated in paragraphs 1-3 that HAADF is the prime tool for pinpointing impurities with Z ≥6 on graphene. We cannot identify hydrogen attached to C-atoms via HAADF, but we will show other means of detecting H in paragraphs 5 and 6. We can identify extensive C-adatom coverage (paragraph 3), and although HAADF contrast evaluation gives strong evidence that the ad-atoms are indeed C (the HAADF signal strength in respective locations is twice that of graphene), due to the error in quantifying weak HAADF signals, we do not want to exclude oxygen atoms as being part of the ad-atom population (although the signal strength in locations of O-adatoms should be ~3x that of pure graphene), nor do we want to exclude, at this stage, the existence of OH-groups. However, we should be able to identify fluorine with a Z number of 9, giving a theoretical HAADF signal ratio F:C of 81:36 and hence an expected HAADF signal strength, in places of F-adatoms, of ~4x that of pure graphene). We have dosed graphene with F (details not given here), however, we could not detect any F retention on pristine graphene patches.
Extensive HAADF investigations, in which we have scrutinised many clean single-layer graphene patches for foreign atoms have revealed it is free of impurities with Z≥9. Graphene investigated for residual impurities was exfoliated by micromechanical cleavage as well as from CVD grown layers on Ni and Cu. Included were also attempts to dope/dose graphene with impurities via metal deposition (Au and Cr).
It should be emphasised that the above said applies strictly to clean, single layer graphene; we have never observed impurity atoms of any kind attached to such sheets. However, we observed many types of impurities in the hydrocarbon contamination on single and multiple sheets, and we did also observe impurity atoms on clean areas in multi-layer graphene.
Transition, noble, and group IV ad-atoms are predicted to modify the graphene electronic states to a large degree indicating covalent bonding with strong hybridization between ad-atoms and graphene. Metal-graphene interactions have been much studied by means of Density Functional Theory (DFT) calculations. H-sites (see fig.12e) are predicted as preferred location for most metals (e.g., Ti, Fe), T-sites for Sb, Sn and Ni, whereas Pd, Cr and Pt are expected to bind strongly to B sites (Suarez-Martinez et al, 2009; Uchoa, Lin & Neto, 2008; Chan, Neaton & Cohen, 2008; Mao, Juan & Zhong, 2008; Sevincli et al, 2008). Experimental exploration of the metal-graphene systems is still limited, especially TEM observations are practically non-existent. Such observation would be of great interest, as calculations have lead to discrepancies in the site of metal atoms: the two common approximation for the calculations, local density approximation and generalized gradient

approximation –the latter does not represent Van-der-Waals forces very well (Leenaerts, Partoens & Peeters, 2008)-, lead to different binding energies and thereby to different sites for Au atoms, T-sites for the former and B-sites for the latter method (Aktürk & Tomak., 2009). In addition, arbitrary variables used in the calculation, such as cut-off energy (Varns & Strange, 2008) and size of the supercell (Leenaerts, Partoens & Peeters, 2009) can affect the result of DFT calculations. It was furthermore found, theoretically and experimentally, that point defects in graphene provide nucleation sites and even further substitutional incorporation of metals (Charlier et al., 2009; Boukhvalov & Katsnelson, 2009; Gan., Sun & Banhart, 2008; Krasheninnikov et al., 2009; Zhou, Gao & Goodman, 2010).

Gold atoms and its dimers on the graphene surface have been studied by using first-principles calculation with the local density approximation (Varns & Strange, 3008). The results show that the gold–gold interaction is significantly stronger than the gold–graphene interaction (for this reason gold is highly mobile on graphene) as is experimentally confirmed by Gan., Sun & Banhart (2008) with observation of gold clusters –rather then atoms- on the graphene sheet. For a single gold atom the favourable energy configuration is found to be directly above a carbon atom. We have evaporated 0.1 nm of gold onto graphene. Figures 11a) and b) show results of such deposition: indeed on single or de-coupled (turbostratic) layers gold atoms do not remain dispersed, but cluster into nano-crystals, and notably, are exclusively located in the hydrocarbon contamination. This demonstrates the extreme mobility of gold on pure graphene. Only in stacked few-layer films (here: exfoliated by cleaving) can single gold atoms be observed: it appears that atoms in sub-surface layers are needed to contribute to the bonding with surface gold atoms in order to prohibit dissociation and diffusion. Figure 11c) is a BF STEM image, and represents phase contrast (like an HREM image). The beam is focussed on the exit surface of the sample; this is the surface, on which the gold is evaporated. So the electron beam proceeds through the graphene layers before it encounters the gold atoms. The aggregate of gold atoms is so thin, that it is invisible in phase contrast, however, the graphene in the BF image exhibits strong contrast and relatively little noise, and shows the lattice periodicities well. This means that for BF analysis the raw (unprocessed) image can be used. Figure 11d) is the corresponding HAADF image, and is obtained simultaneously with the BF image. The image intensity arising from incoherent elastic scattering of few atom layers is very much lower than in BF, and the noise is so high that the benzene rings are barely recognisable. However, the gold atoms are clearly visible. They have formed a loose aggregate with single atoms dotted around the aggregate, some of which we have numbered. We note that comparing identical positions in images (c) and (d), the benzene ring centres, known to be black in HAADF images, correspond to bright patches in the BF images; this can be seen from the schematic benzene rings (red) overlaid on the HAADF image and positioned in identical locations in the BF image. Hence the C-atoms surrounding the black centres in HAADF images, constituting bright contrast, correspond to dark contrast in BF images. Due to the weak contrast and the noise of the raw HAADF image, although gold atoms can be located rather accurately, it would be near impossible to assign them exact sites on the benzene rings. However, the benzene ring shape is clearly discernible in the BF image, and by locating the exact corresponding position here (circled), the sites can be identified. It thus occurs that all gold atoms sit on T-sites. This is in agreement with theoretical predictions.

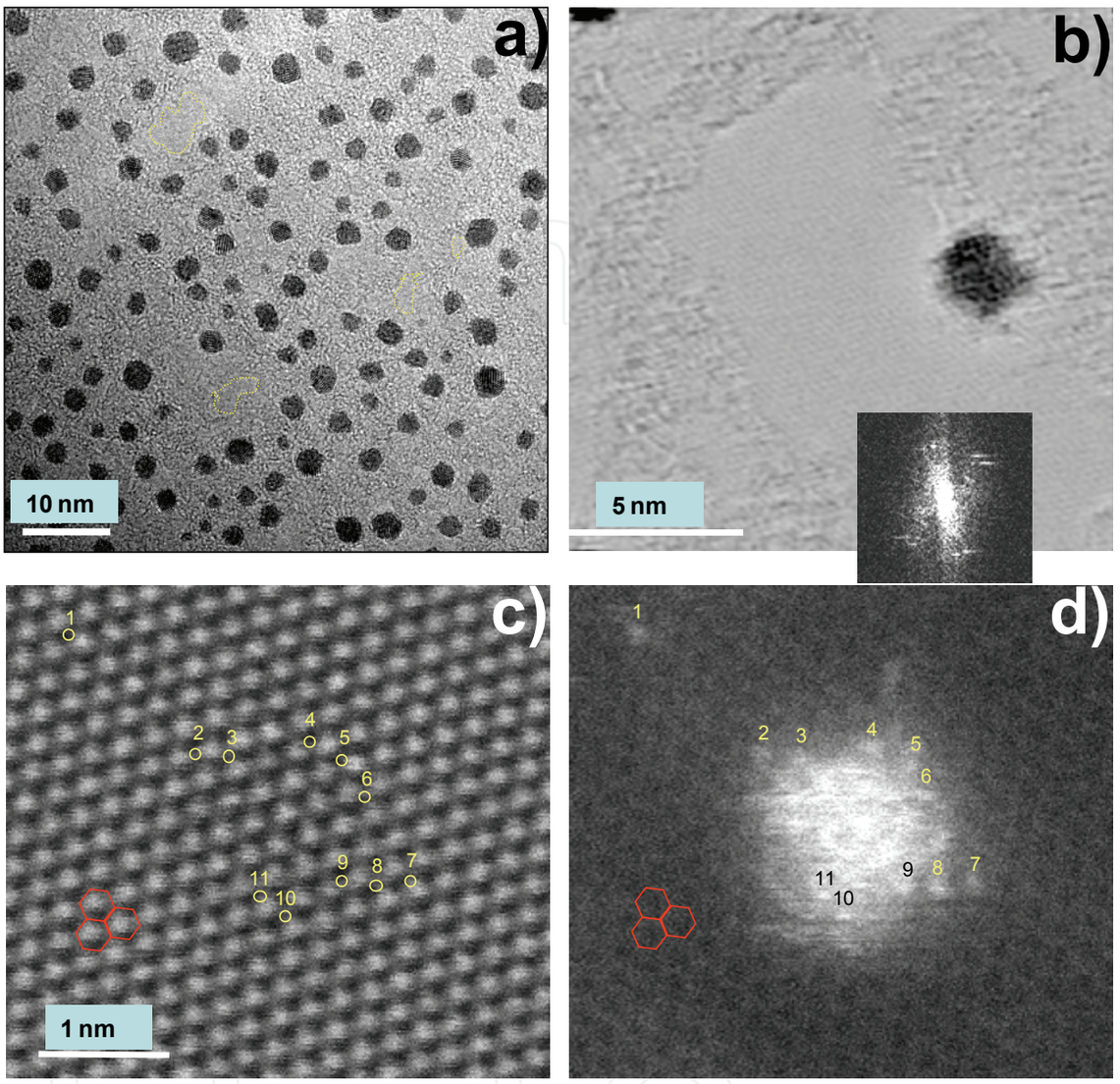

Fig. 11. a) TEM image of 0.1 nm gold evaporated on mono-layer graphene, b) BF STEM image of 0.1 nm gold evaporated on 2-layer turbostratic graphene with FFT of the image as inset to show, by the double spots, that the two layers are rotated with respect to each other, c) and d) BF and HAADF STEM lattice image of the same area in few-layer graphene. Here individual gold atoms can bee seen separated from the small cluster in the middle. Identical positions of the benzene rings are marked in red, showing that bright contrast in the BF image corresponds to the dark, hollow centres of benzene rings in the HAADF image. Single atoms 1-11 are marked with the numbers occurring just above the atoms in the HAADF image; identical places are marked by yellow circles in the BF image, showing that Au-atoms sit on T-sites (see fig. 12e) on the sample surface. All images represent raw, unfiltered data.

Iron-atoms have not been deliberately deposited, but reside as impurities on many samples, presumably as a result of chemical processing. The graphene sample in the here presented results was obtained by micromechanical exfoliation. Figure 12a) shows again that on uncontaminated single layer areas (black patches) the sticking probability is very small: all Fe clusters and single atoms (white spots) are located on hydrocarbon contamination (greyish areas). On the surfaces of multi-layer graphene on the other hand individual atoms can be seen. Figures 12c) and d) are HAADF and BF images of 1-4-layer staggered graphene sheets; with the sheet number increasing from the right to the left (i.e., on the right edge of the image is one sheet). Fe-atoms are clearly visible in (c) and corresponding positions have been circled in (d). The spectrum on the right of fig. 12c) is an energy loss spectrum taken on an individual Fe-atom, showing the characteristic $L_{2,3}$ absorption edge of Fe at ~708 eV. In fig.12b) the areas around two Fe-atoms are enlarged with a model of the AB-stacked graphene lattice overlaid. From this it becomes clear that the Fe-atoms in both cases sit on B-sites. This contradicts calculations, which predict H-sites.

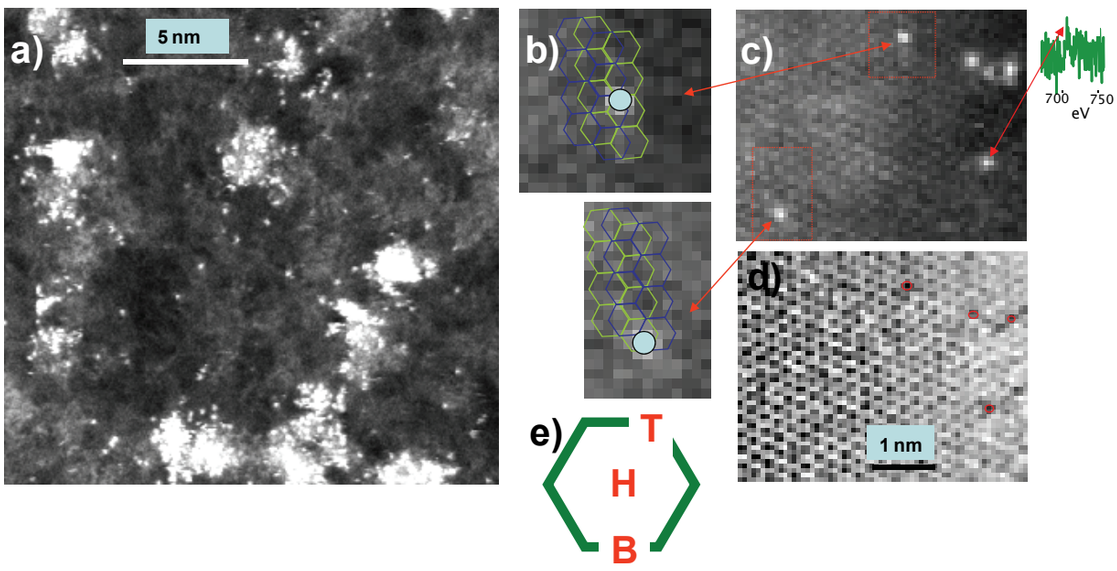

Fig. 12. a) Fe-atom contamination on single layer graphene, showing that all Fe- impurities sit on hydrocarbon contamination and not on clean graphene patches, b) enlargement of the red framed areas in the atomic resolution HAADF image of few-layer AB-stacked graphene in (c). The model of the lattice and positions of the Fe-impurity atoms are overlaid, c) HAADF image of larger area showing individual Fe-atoms on few-layer AB-stacked graphene. The inset on the right hand side of (c) shows an EEL spectrum with Fe $L_{2,3}$ absorption peak, taken on the arrowed atom. d) BF STEM lattice image of the same area as in (c); positions identical to those of atoms in the HAADF image in (c) are circled in red. The graphene sheets are staggered starting with a single sheet with on the right, followed by a second, third and fourth sheet towards the left with edges running parallel to the sides of the frame. e) model of benzene ring with sites of impurity atoms.

Nickel-atom contamination is shown in figure 13. The graphene film in this case was grown by CVD on Si with a sacrificial Ni-layer on top of the Si-substrate. Ni-atoms have remained 'stuck' to the film after lift-off. The image in this example is a low-pass filtered HREM phase contrast image taken in a TEM. The large underlying image shows mono-layer Ni-atom islands or –rafts on top of graphene, which itself consists of a patchwork of 1 and 2 layers and more.

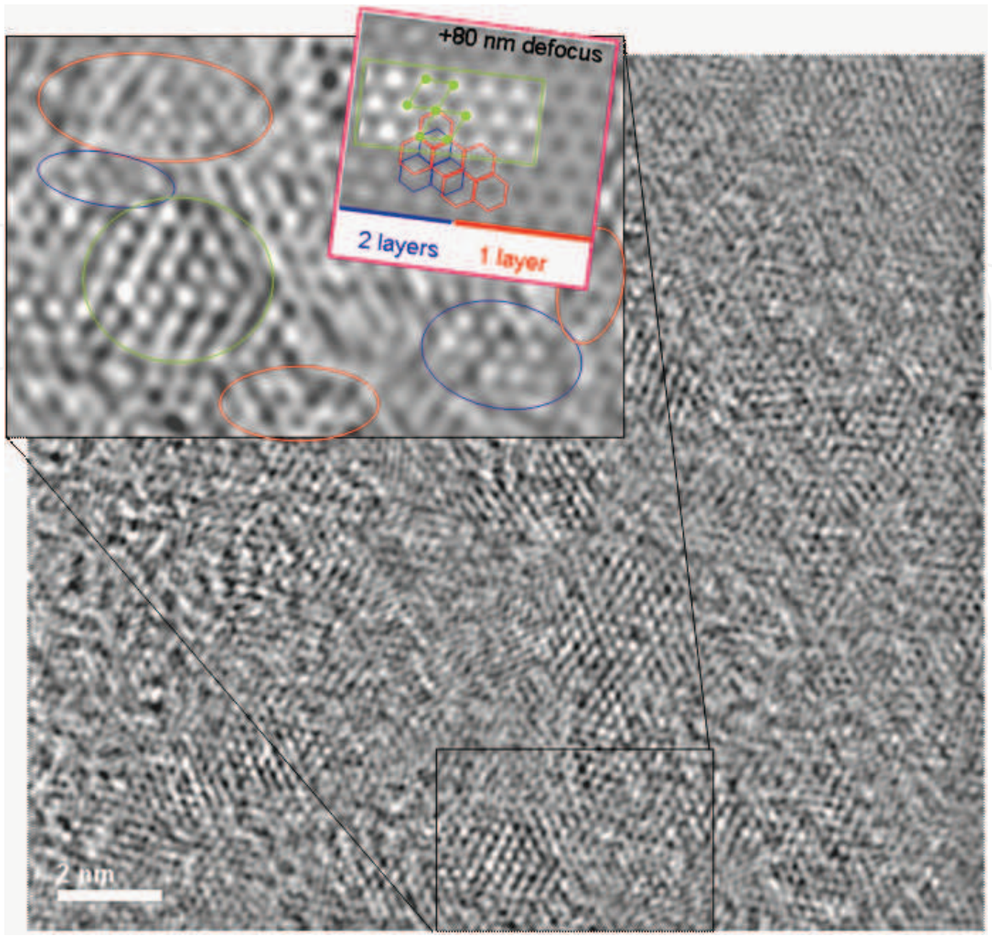

Fig. 13. Low pass filtered HREM image, taken in a TEM, of graphene grown by CVD on a sacrificial Ni-layer on Si. The area in the image consists of patches of mainly mono- and bi-layers, as well as of mono-layer Ni-islands. The larger inset is an enlargement of the black-framed area, the smaller inset is an image simulation, using the TEMSIM program, of mono- and bi-layer graphene with a mono-layer island of Ni stretching over both. Features with similar contrast in the experimental image in the larger inset are circled with the respective colours. The focus value of +80 nm achieves strongest contrast of Ni and graphene simultaneously.

The contrast in phase contrast images is not straight-forwardly interpretable and depends on sample lens aberrations, sample thickness and defocus, and it is common practice to run image simulation., if information other then that about lattice periodicities and perfection is to be extracted. We have used the TEMSIM code (Kirkland, 2005). The small inset shows simulated HREM contrast for 1 and 2 layers and a Ni-atom island covering parts of both, the single and the bi-layer. The model lattice for the graphene layers (red and blue) and a Ni-atom raft (green) is overlaid. The simulations were run for a series of focus values; we have depicted the simulation for 80 nm defocus, as this focus condition achieved the strongest contrast (best visibility) in the simulated images, so this value would be 'automatically' tuned to in the experiment. It should be noted that in overfocus conditions Ni-atoms have bright contrast similar to the centres of benzene rings in 2-layer graphene, whereas in 1-layer graphene the

centres of benzene rings are dark. Comparing this to the larger inset, which in turn is an enlargement of the black famed area in the underlying image, we can then identify single layer (circled in red) and bi-layer (circled in blue) patches. Atoms constituting a Ni-island (circled in green) can be recognised by their strong, bright contrast (like in the image simulation). In relationship to the C-hexagons the position of these Ni-atoms can be assigned T-sites in benzene ring in agreement with above mentioned calculations.

5.2 Impurities with Z≤ 6

Interesting potential electronic dopants in graphene, such as nitrogen and ***boron***, due to the similarity in atomic number with carbon, cannot easily be detected in HAADF images. However, their presence, and even local bonding environment, should be accessible via core loss EELS. With probe aberration corrected STEM it is possible to detect EEL signals and positions of single atom (we have already shown an example of this in fig. 12c). Boron was ion implanted at 100 eV to a level giving on average one atom per nm² (10^{14}cm^{-2}) (Bangert et al., 2010a) Figure 14a) is an atomic resolution STEM BF image of few-layer graphene. A spectrum image was taken over the whole image area, and pixels, in which B K-edge signals were detected, are filled in yellow. Although the dopants appear dispersed the retention is less then 10%. We do presently not have an explanation as to why the retention is so small, other then that the implantation energy might not have been large enough to incorporate B in the lattice. This might have been the case, since Pomoell et al. (2003) estimate that ions ranging from carbon to xenon loose on average 300 eV when penetrating a single walled CNT, i.e., 150 eV per graphene sheet. Figure 14f) shows EEL spectra of the B K-edge, extracted from the yellow pixels. Although noisy, the spectra exhibit a sharp peak at 192 eV, which very much resembles the π*-peak spectra of boron-doped carbon nanotubes measured by Fuentes et al. (2003), indicative for substitutional boron.

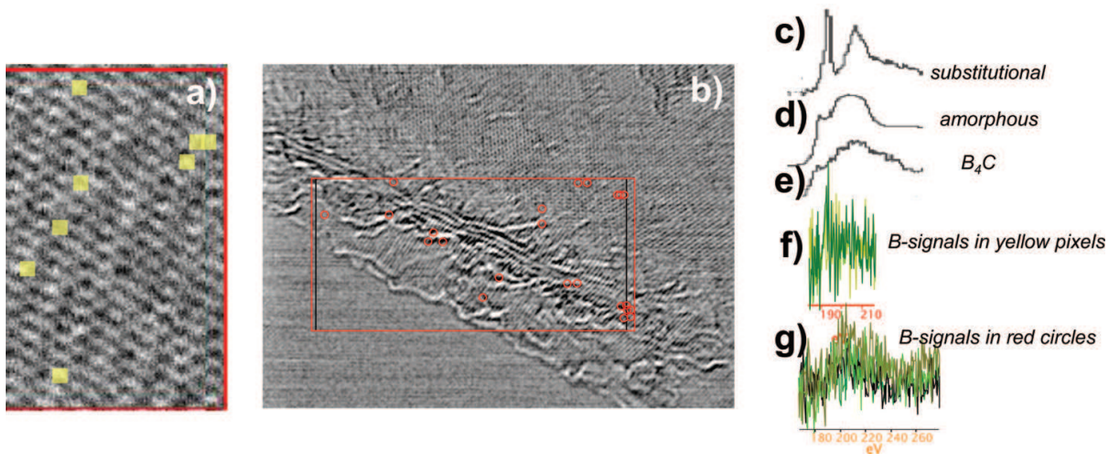

Fig. 14. a) STEM BF image of few-layer graphene and b) of staggered graphene sheets, starting with a single sheet, whose edge runs diagonally from left side to bottom right, implanted with B to a dose of 10^{14} atoms cm^{-2} at an energy of 100 eV. Positions were B K-edge EEL signals were recorded in spectrum images (area indicated by red frames) are indicated by yellow squares (a) or red circle (b), c) literature reference spectrum of BN (Gatan EELS atlas), d) of amorphous B, e) of B_4C, f) spectra extracted from yellow pixels in (a), g) spectra extracted from red circles in (b).The spectra in (f) and (g) indicate that B assumes substitutional positions in multilayers, and attaches along graphene edges in form of few-atom clusters.

Interestingly, the rather strong B-signal obtained from staggered graphene sheets in fig. 14g) does not exhibit the π*-peak. Signal positions are indicated by red circles in fig.14b); they coincide in most cases with the edge of graphene sheets: the leftmost portion of the image in 14b) represents a single layer, followed (towards the right) by the 'frayed' edge of a second sheet along which a number of signal positions are marked. This edge is followed by, to a large part, straight edges of four further graphene sheets, with a cluster of boron signal positions marked at the bottom left hand corner of the image, and two further positions higher up along these edges. Typical spectra of the boron K-edge in red-circled pixels are shown in fig. 14g). Comparison with spectra of amorphous boron (fig.14d) and B_4C (fig.14e) suggests that small few-atom boron clusters have formed attached to sheet edges or mono-atomic steps. Hence, although there is indication of substitutional B-incorporation via low energy ion implantation in few and many-layer samples (as in the case of carbon nanotubes (Bangert et al., 2010a), B does not seem to substitute atoms in single, bi- or triple-layers, nor does it appear bound to the surface. As in the case of metal impurities in previous examples mobilities of single-atom species on graphene surfaces seem very high.

The possibility for ***atomic hydrogen*** to be chemi- or physisorbed on graphite surfaces (Jeloaica & Sidis, 1999) and graphene has been researched theoretically and experimentally (e.g., Ito, Nakamura & Takayama, 2009; Elias et al., 2009), and direct experimental observation has been attempted via transmission electron microscopy imaging (Meyer et al., 2008b). H-dosing appears promising for band-gap engineering of graphene. In order to carry out investigations of the effect of hydrogen on the graphene atomic and electronic structure we have dosed graphene with hydrogen by exposure to a hydrogen plasma, described in Elias et al., (2009).

H cannot be revealed in HAADF images, so in order to assess H adsorption on graphene we have carried out EELS. Figure 15a) shows low loss spectra, which were obtained of uncontaminated graphene patches, typically a few 10 nm^2 in size. The blue spectrum in (a) is a reference spectrum taken of pristine, hydrogen-free graphene. To ensure that we have hydrogen-free surface areas few-layer graphene regions were repeatedly scanned in the STEM. The scan raster was successively decreased, and HAADF images in combination with EEL measurements revealed material being peeled off layer-by-layer, until finally a hole appeared. The blue spectrum is from the last remaining layer after such a repeat-scan procedure; the Lorentzian fit curve (red dotted line) was obtained from least squares fitting, and was used as fit for the rise of the σ+π plasmon. Spectra of such freshly revealed areas did not show the bump at 13 eV like in the orange spectrum above, which was obtained from a deliberately hydrogen dosed sample.

We applied the spectrum imaging method (Jeanguillaume & Colliex, 1989), and scrutinised entire EEL-spectrum images for occurrence of the ~13 eV core-level excitation signal of hydrogen. Spectrum images were obtained in the following way: a raster was defined over an area of an uncontaminated patch and in each pixel (typically 0.3x0.3nm^2) of this raster a spectrum was taken. Intensity maps, extracted from these spectrum images are shown in figs 15b) and c). These maps were obtained by displaying in each pixel the intensity of the respective spectrum integrated over an energy window ~12-14 eV, after having subtracted the plasmon background determined by the Lorentzian fit. These maps represent the distribution and relative amount of hydrogen on the graphene surface. Since spectra from individual pixels display a great deal of noise, we carried out Principle Component Analysis (PCA) on the spectrum images prior to background subtraction (e.g., Borglund, Astrand & Csillag, 2005). This reduces the noise significantly, and clearly reveals the bump on the rise of the σ+π plasmon at ~ 13.2 eV as seen in the orange curve in fig.15a).

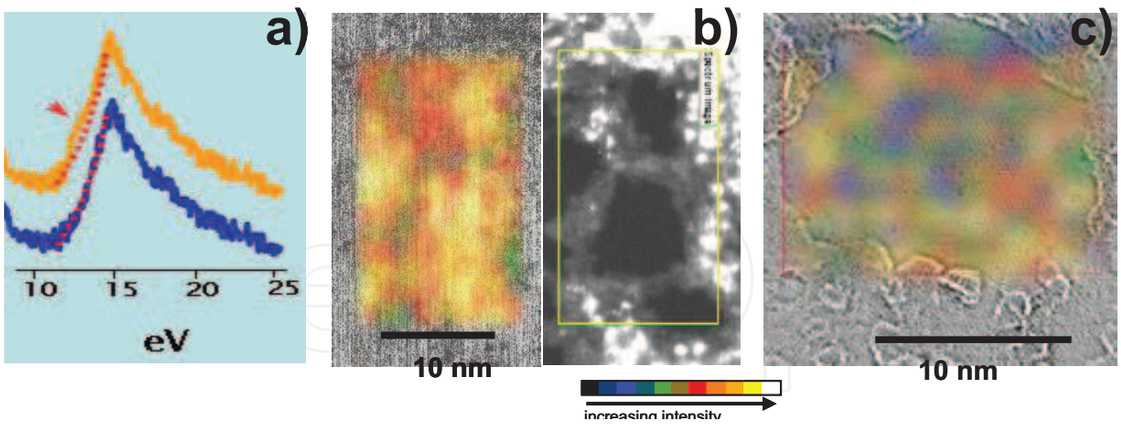

Fig. 15. a) low loss EEL spectra showing the π+σ-plasmon of ***H-free*** (electron beam 'zapped') single layer graphene with Lorentzian fit (blue spectrum) and of hydrogen-dosed graphene with the same Lorentzian fit-curve (orange spectrum), b) EEL intensity map of hydrogen-dosed graphene, showing the integrated intensity –after Lorentzian background subtraction- in the energy region 12-14 eV; the map is overlaid on the respective STEM BF image area (left); the corresponding HAADF image is shown on the right, c) EEL intensity map of pristine, i.e., undosed graphene, obtained with the same procedure as in (b), overlaid on the respective STEM BF image area.

Figure 15b) shows an EEL intensity map of the H-core loss signal of hydrogen-dosed graphene. The intensity map is overlaid on the BF STEM image area where the spectrum image was taken. The corresponding HAADF image is also shown. It reveals a hydrocarbon 'net' (greyish contrast), bordering uncontaminated single layer graphene patches (black), as well as contaminants of higher atomic number (white dots) on top of hydrocarbons. The intensity map shows highest H-signals (yellow/orange) in regions free of hydrocarbons, whereas hydrocarbon contamination shows up with lower intensity values (green). The reason for this is that hydrocarbons with longer chains have a distribution of energies of the molecular orbitals causing a spread in the H-core level energies with a shift towards lower values (Murell & Schmidt, 1972). These will not have been picked up in the energy window set for the intensity map in (b). Figure 15c) shows an intensity map obtained with the same energy window of 12-14 eV in an uncontaminated region in pristine graphene, revealing that hydrogen is present on clean graphene even without hydrogenation. Again the map is overlaid on the STEM BF image. The amount of hydrogen, however, is significantly lower (by 2-3 times) then in the dosed sample, as evidenced by the colour-scale. A detailed discussion of hydrogenation studied by EELS can be found in (Bangert et al., 2009b).
The question about coverage, detailed atomic structure and bonding arrangements of the hydrogenated areas poses itself. We can get a fair insight into this via highly spatially resolved valence band EELS, i.e., EELS in the extreme low loss regime in combination with DFT calculations; an introduction into this will be given in paragraph 6.

6. Plasmons in graphene: indicators of local electronic bandstructure

6.1 Pure graphene

From an experimental viewpoint, an essential task in the research into 2D structures is to provide evidence that they do indeed exist. This is especially important, because theory does not allow the existence of perfect crystals in 2D space. STM-, AFM- and Raman studies have

given indirect proof of the existence of single-layer graphene. The most conclusive evidence for the existence of *free-standing* graphene, except for the HAADF studies reported in Bangert et al. (2009b) and Gass et al. (2008), a resumé of which has been given in paragraph 3, has been obtained from electron diffraction experiments (Meyer et al., 2007a).

By carrying out highly spatially resolved electron energy loss spectroscopy (EELS), we observe significant red-shifts in the frequency of plasmons in sample positions concomitant with single graphene sheets (Eberlein et al. 2008), very similar to those observed in SWCNTs (Stéphan et al., 2002). Surface plasmon behaviour in thin metal sheets is well documented experimentally and explained using dielectric theory (Raether, 1977; Otto, 1967). There are also numerous reports on surface plasmons in graphite and carbon nanotubes (Annet, Palmer & Willis, 1988; Laitenberger & Palmer, 1996; Perez & Que, 2006; Kociak et al., 2001).

A characteristic of thin foils is the vanishing of the bulk plasmon mode, leaving only the surface plasmon mode; the out-of-plane and in-plane contributions of the latter split in energy when the product of foil thickness d and plasmon momentum q, tends to zero; in graphite the maximum/minimum energy of the π -> π* transition tends to roughly 7 and 5 eV, and of the σ-> σ* transition to 20 and 15 eV, respectively (Stéphan et al., 2002). The $\boldsymbol{E}$-field of a fast moving particle is elongated along its direction of travel, therefore, when passing perpendicularly through a graphene foil mainly the out-of plane mode, with momentum $\boldsymbol{q}$ parallel to $\boldsymbol{E}$, should be excited. However, these modes are forbidden in a single layer (Eberlein et al. 2008), and they have weak intensity in graphite. In an EELS experiment carried out in a STEM, although the momentum transfer is close to zero, nonetheless, $\boldsymbol{q}$ has a considerable in-plane component (along $\boldsymbol{a}$, the in-plane spacing) because the collection angle is several mrad. For this reason we will observe surface and bulk plasmons excited with $\boldsymbol{E}$ (or $\boldsymbol{q}$) parallel to $\boldsymbol{a}$.

Graphene samples for the plasmon studies were obtained by exfoliation after micromechanical cleavage. An HAADF image of a region including one to up to a few graphene layers is shown in Fig. 16a), top panel; the narrow, rectangular bar shows the line along which the intensity (overlaid profile), integrated over the width of the bar, is traced. The step heights in the contrast profile are multiples of the smallest height at position 1 (to the right of which is vacuum), confirming that the contrast in this location arises from one single graphene sheet.

Plasmon spectra taken in positions near the edges of one, two, three and several sheets (fig.16a, bottom panel) show that the π-mode, at 7 eV in graphite, has shifted to 4.8 eV at position 1 relating to single graphene layer. Furthermore, the spectrum here exhibits only the π+σ -surface mode at 15 eV and the 26 eV bulk mode of graphite is not present. The shape and intensity of the one-layer plasmon structure was repeatedly measured in different places on the same sample, in different samples and even in different experimental sessions. Given the same acquisition conditions (e.g., energy dispersion, electron beam current and dwell time), nearly identical spectra were obtained, which at the same time, constituted the lowest plasmon signal measured overall. For two sheets the triangular shape of the π+σ resonance gives way to a plateau and the integrated intensity under the peak approximately doubles, for three layers it triples; this linear relationship carries on up to ~8 layers, but for increasing numbers of sheets, features above 15 eV start to appear and the plasmon maximum moves to higher energies accompanied by further broadening. The multi-layer plasmon structure in fig.16a) strongly resembles that of graphite. The plasmon characteristics are thus supreme indicators for the presence of single layers.

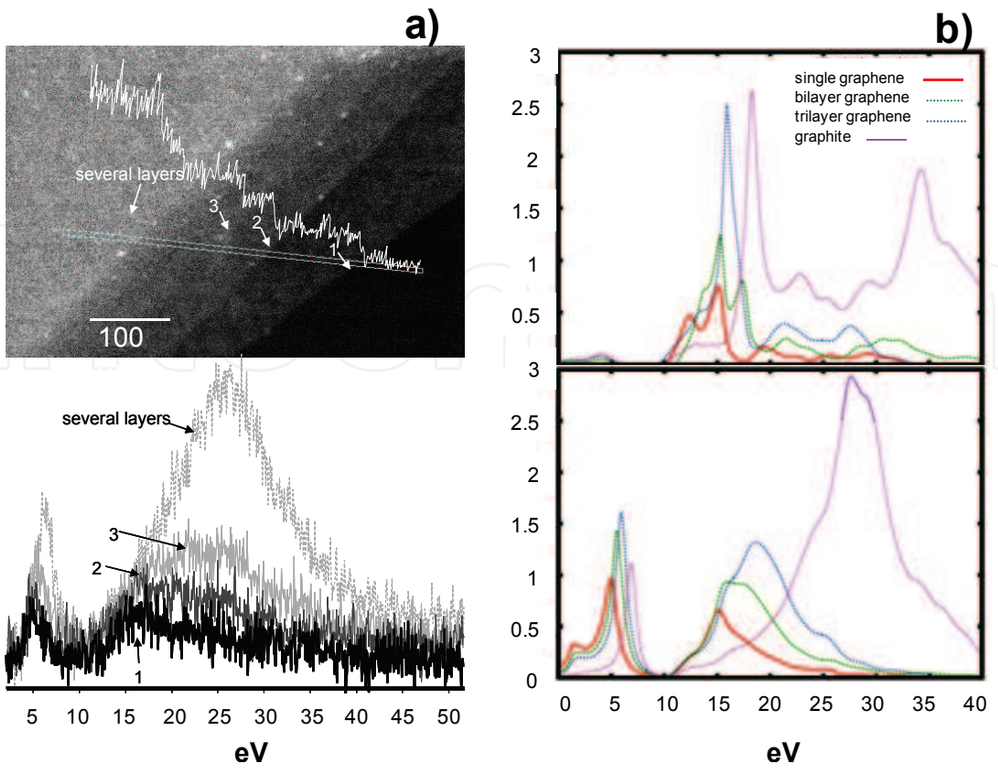

Fig. 16. a) top panel: HAADF image of staggered graphene layers with overlaid intensity profile, which was taken in the turquoise box. The arrows indicate the positions of the edges of new layers, the bottom right corner is vacuum; bottom panel: b) EEL spectra taken of one, two, three and six layers, showing the π- and the π+σ-plasmon shifting to higher energies with increasing layer number; b) AIMPRO calculations of EEL spectra of single, bi- and triple-layer graphene and of graphite for ***E***-fields (plasmon ***q***-vectors) parallel to the ***c***-axis (top panel) and parallel to the graphene sheet (bottom panel). The latter spectra show good agreement with the experimental spectra, indicating that the plasmons in graphitic structures are in-plane plasmons.

In support of the experimental results we have carried out EEL spectra calculations using the AIMPRO local density functional code (Jones et al., 2000; Fall et al., 2002) to evaluate the imaginary part of the dielectric tensor for q=0 and use the Kramers-Kronig relations to derive its real part. The loss function is then found for graphite, graphene and bi- and tri-multilayers. We have also carried out density functional calculations using the WIEN2K code (Nelhiebel et al., 1999), (results of this are shown in the last part), and, after optimising the input parameters and obtaining convergence, acquired identical results as with AIMPRO.

In modelling physical properties of extended periodic (e.g., crystalline) structures the desired process is applied to a unit cell of the structure and the 'outcome' for the entire sample obtained by assembling unit cells in a 3D repeat operation. The representation of nano-objects by repetition of a crystallographic unit cell within the nano-object is inappropriate (the object itself may only consist of few unit cells), here the usual approach is to build large 'supercells' with the entire structure of the nano-object placed in the middle surrounded by vacuum. A repeat structure of these supercells is then obtained and the

calculations carried out as described above. If the supercell is large enough, the calculations of individual unit cells do not impact on each other and the modelled physical property represents that of the supercell alone. To find the required size of such a supercell is tricky, and often a series of calculations for increasing size is carried out until the 'outcome' converges.

Graphene, was modelled by expanding the lattice parameter along ***c*** (Eberlein et al., 2008); convergence occurs at around 20 lattice parameters in this direction, but qualitative changes in the low loss spectra already cease to happen at 5 ***c***-parameters. Figure 16 b) shows calculated spectra for single, bi- and triple-layer graphene for plasmon propagation (momentum vectors) ***q*** along the ***c***-axis (top panel) and in-plane (bottom panel). Notably in single layers (red line) the loss for ***q*** | | ***c*** is almost zero up to 12 eV, and after this the onset occurs at a similar energy to graphite. However, the peak heights are very different from graphite. The disappearance of the 4 eV peak can be explained by a selection rule. As stated above the peak is due to a transition between occupied and unoccupied π * bands at the M (1/2,0,0) point of the Brillouin zone. (Inspection of the wave functions for these two states shows that both transform as ***pz,*** and are odd under the reflection symmetry present in the basal plane of graphene, but not AB graphite, and hence the dipole matrix element between them vanishes for transitions for which ***q*** is parallel to ***c,*** although the transition is allowed for ***q*** parallel to ***a***.) This shows that the dielectric constant of graphene is not the same as graphite. Fig. 16b), bottom panel, compares the loss function for ***q*** | | ***a*** for graphite and graphite. We note there are substantial red-shifts of the peaks found in graphite (Eberlein et al., 2008). The 7 eV plasmon peak has shifted downwards to about 4.8 eV while the broad peak around 27 eV has sharpened and shifted to 14 eV just as seen in the experimental spectra; in fact the latter seem to be entirely dominated by the in plane plasmon component (***q*** | | ***a***). The loss functions for bi-layers, triple-layers stacked as in graphite, and graphite itself are shown as green, blue and purple curves. The separation between periodically repeated multilayers was chosen as 5 times the separation in graphite. The supercell containing the trilayer for example, has three layers of graphene separated by the interlayer separation found in graphite, but the separation of these planes from similar planes in adjacent unit cells along the c-axis is now 5 times the separation in graphite. The peak positions depend on the number of layers. There is an increasing red shift of the π+σ plasmon resonance as the number of layers decreases. Markedly, there is also a red-shift to ~4.7eV in the graphitic π-plasmon, the latter only occurs for ***q*** | | ***c*** (see bottom panel 16b). The relative amplitudes of the two plasmon peaks here for the different layers seem roughly consistent with experimental spectra in Fig.16a).

It is the π-plasmon, which bears significant information about electronic properties of graphene and is especially sensitive to modifications of graphene. In the last sub-paragraph we will give a glimpse of the wealth of properties of graphene that can be deduced from the π-plasmon.

6.2 π-plasmon in modified graphene

To give an example of the sensitivity of the low loss region to modification of graphene we return to the hydrogenation issue. In paragraph 5 we observed presence and distribution of hydrogen atoms by their core level excitation, but the detail of the atomic-scale structure was not revealed; questions concerning issues that might have implications for electronic properties include: Is hydrogenation complete? If not, is there ordering of H-atoms? Is H

bonded on both sides? If not, does this induce strain (Xue & Xu, 2010)? Does hydrogenation induce diamond-like, corrugated atomic stucture (Sofo, Chaudhari & Barber, 2007; Elias et al. 2009)?

In all spectra, which showed the H-core loss signal, additional structure was found in the low loss region on the high energy tail of the π-plasmon. Experimental low loss spectra of pure and of hydrogenated graphene, including the π-plasmon, can be seen in figures 17a) (purple curve) and 17c) (orange curve). An extra peak at ~7eV has occurred in the latter, whereas the pre-plasmon peak at ~2eV in pure graphene has vanished. EEL intensity maps of the integrated intensity (after subtraction of a fitted plasmon tail) in the 6-8 eV region, from the same area as in fig. 15b show identical intensity distributions as seen in the latter figure. This suggests that the 7-eV feature is induced by hydrogen. More interestingly, the π-plasmon remains present throughout the spectrum image, in co-existence with the new feature, which is similar to a feature occurring on unpassivated, reconstructed diamond surfaces (Bangert et al., 2006), which have undergone reconstruction of their dangling bonds into π-bonded chains. Hydrogenation ought to passivate the π-bonds, and cause formation of sp^3 bonds instead, and hence dramatically diminish the occurrence of the π-plasmon. However, the π-plasmon in graphene exposed to a hydrogen plasma is nearly undiminished in areas, which, at the same time, show the H-ground state excitation. Co-existence of the π-plasmon and the 13.2 eV signal suggests that hydrogenation is not complete, i.e., not every C-atom is bonded to an H-atom.

In order to support the above interpretation of the EELS observations and to reproduce the EEL spectra theoretically, DFT calculations using the WIEN 2K code, have been performed. WIEN 2K is an all-electron code and uses the General Gradient Approximation with a mixed linearized augmented plane basis set of wave functions (Nelhiebel et al. 1999; see also Blaha et al. 2010). There is a fair number of bandstructure calculations of hydrogenated graphene in the recent literature, predicting the opening of a band-gap of ~3.7 eV and C atoms displaced from planar geometries by H atoms (e.g., Haberer et al., 2010), optimum corrugation angles and resulting bandstructure (Sofo, Chaudhari & Barber, 2007), and influence of hydrogenation on strain and corrugation angle (Xue & Xu, 2010).

As mentioned before WIEN2K calculations carried out on graphite and pure graphene show identical results to those from ab-initio calculations using the AIMPRO code, which reproduces measured spectra very well (Eberlein et. al. 2008) This gives us confidence in using WIEN calculations –not previously applied to graphene- on hydrogenated structures. It is beyond the scope of this chapter to go into detailed discussion of the input parameters and how they were established; it suffices to say here that all parameters (k-point number, maximum g-vector, muffin tin potential radius) were the minimum value requirements for convergence of the calculations to occur, and that a detailed discussion of the procedures and the results of WIEN calculations of hydrogenated graphene can be found in Bangert et al. 2010b.

Also shown in figure 17a) is a calculated EEL spectrum for single-layer graphene. It matches the experimental spectrum very well. Surprisingly flat and corrugated unhydrogenated graphene both produce similar π-plasmons, indicating the presence of a π-electron system even in corrugated graphene. Figure 17b) shows the evolution of the π-plasmon in fully hydrogenated graphene (also termed graphane) with increasing corrugation angle. Interestingly, flat graphane, similar to graphene, possesses a π-plasmon. However, its energy is slightly higher then experimentally observed. The π-plamon has nearly vanished

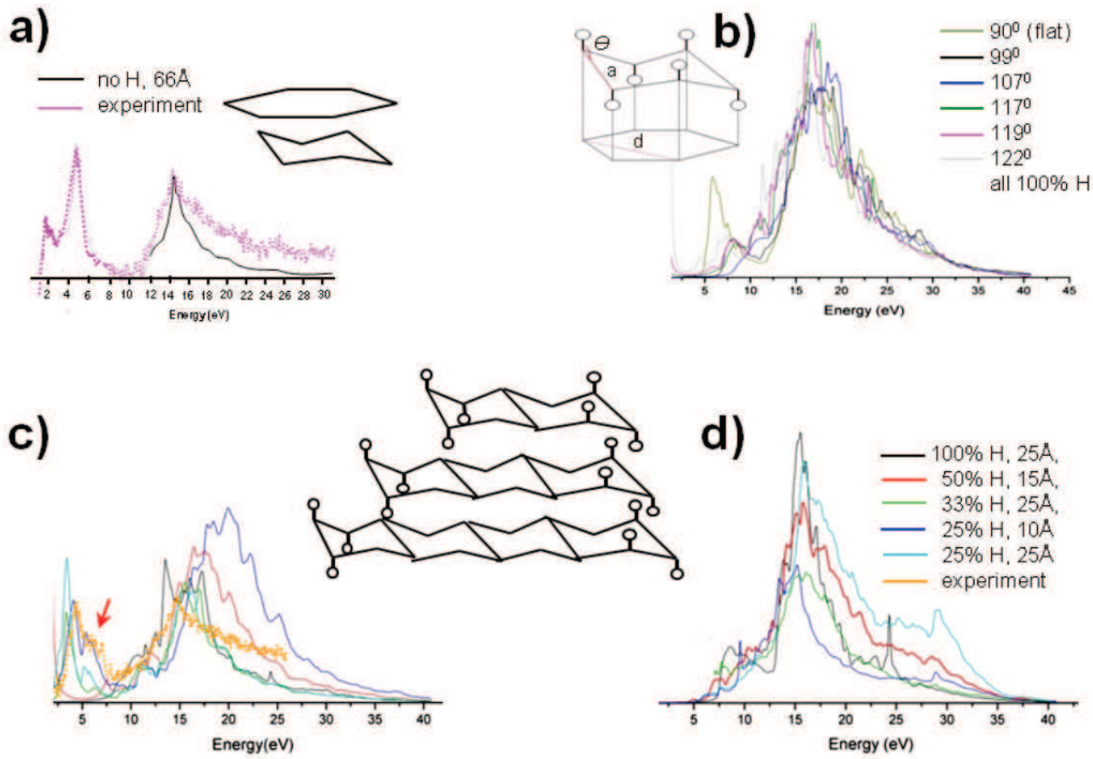

Fig. 17. WIEN 2K calculations of low loss EEL spectra for a) non hydrogenated graphene in flat and corrugated geometry for the in-plane plasmon component ($q||a$) with overlaid experimental spectrum. Note the agreement in the pre-plasmon structure; b) fully hydrogenated graphene with varying corrugation angle Θ, again, for ($q||a$). c) and d) show calculated in-plane and out-of-plane ($q||c$) plasmon components for corrugated graphene (Θ=114^0) with different hydrogen content (given in % in the legend; model structures are shown in the sketch). The orange spectrum overlaid in (c) is an experimental spectrum of a hydrocarbon-free region in H-dosed graphene. Note the disappearance of the pre-plasmon feature and the occurrence of an extra peak at ~7eV. The distances given in Å in the legends are the separation distances of the graphene sheets, or the supercell dimension along the c-axis. Further detail and fuller explanation of the input parameters (k-point number, muffin-tin radii etc) are given in Bangert et al. 2010b.

for 10^0 out-off-plane bending of bonds, and has disappeared for 22^0 bond bending. A feature at ~6-7 eV emerges at the rise of a (presumably) pure σ-plasmon, which sits at slightly higher energy then the π+σ-plasmon in graphene. Hence sp^3 character does become established in corrugated graphene, when all bonds are used. It should be noted that (a) and (b) show the in-plane plasmon component. Figures 17c) and d) show plasmon calculations of the in-plane and the out-off-plane plasmon component for different hydrogen coverages for a sheet corrugation angle of 114^0 (as deduced from diffraction experiments (Elias et al, 2009)). The overlaid experimental spectrum fits the >25% hydrogenation cases rather well. The out-off plane component does not have a π-plasmon for any hydrogen coverage. Models to describe possible structural scenarios are shown as inset. It becomes clear that corrugation is essential to produce the ~7eV feature, as is occurrence of sp^3-character. In order be preserve π-bonding, however, the corrugation angles have either to be small (as

would be the case for strained graphene, if it is hydrogenated mainly on one surface (Xue & Xu, 2010)) or unhydrogenated areas have to be present,. Alternatively or simultaneously, hydrogenated patches could be interleaved with pure graphene areas. The low loss region thus provides a wealth of information, which we have only just started to explore.

7. Acknowledgements

We gratefully acknowledge our colleagues from the University of Manchester, A. Geim and K. Novoselov for stimulating discussions and R. R. Nair for provision and hydrogenation of samples. We thank Q. Ramasse from the SuperSTEM for conducting the Au-on-graphene STEM measurements and J. Vandenberg from Salford University for the low energy ion-implantations.

8. Conclusions

Combined HAADF/BF imaging in an AC STEM has proven a most powerful method to 'see' directly the atomic-scale landscapes of graphene; the former imaging mode provides chemical information and position of atoms, the latter, due to the stronger contrast, helps relate positions of ad-atom/ impurities with sites on benzene rings. Ultra-high resolution EELS has proven an invaluable add-on to identify the chemical nature of individual atoms, especially those with $Z \leq 6$, and to gain information about local bonding and electronic bandstructure.

The imaging studies revealed extensive hydrocarbon contamination on every single graphene sample, independent of growth method or fabrication procedure, as well as a fair proportion of multiple layers and –in CVD grown samples- predominance of turbostratic arrangements. Here we present facts concerning uncontaminated ('model') graphene, which exists in patches of only few 10s of nm in diameter interspersed with extended chain-like adsorbate networks. In 'model' graphene we have shown existence of nanometer-size ripples, point- and ring defects and omnipresence of C-adatoms above C-C bonds. We have identified metal impurity sites and found Au- and Ni-atoms taking up T-sites on benzene rings, and Fe-atoms to occupy B-sites; the former in agreement with and the latter contradicting theoretical predictions. H can be found on clean graphene, and to a much larger extent on hydrogen-dosed graphene. EELS in combinations with DFT WIEN calculations shows the structure of the latter is concomitant with corrugated graphene possessing partial H-coverage and small corrugation angles, or/and co-existence of unhydrogenated areas. Plasmons in graphene show unique behaviour and can be used to identify single layers.

9. References

Annet, J. F., Palmer, R. B & Willis, R. F., 'Surface dielectric response of a semimetal- electron energy loss spectroscopy of graphite', *Phys. Rev. B* 37, 2408-2414 (1988)

Aktürk, O.Ü. & Tomak, M., 'AuPt clusters adsorbed on graphene studied by first-principles calculations', *Phys. Rev. B* 80, 085417 (2009)

Bangert, U., Barnes, R., Hounsome, L. S., Jones, R., Blumenau, A. T., Briddon, P. R., Shaw, M. J. & Öberg, S., 'Electron energy loss spectroscopic studies of brown diamonds' *Phil Mag* 86 (29-30), 4757-4779 (2006)

Bangert, U., Eberlein, T., Nair, R. R., Jones, R., Gass, M. H., Bleloch, A. L., Novoselov, K. S., Geim, A., Briddon P. R., 'STEM plasmon spectroscopy of free standing graphene', *phys. stat. sol. A* 205 (9), 2265-2269 (2008)

Bangert, U., Gass, M. H., Bleloch, A. L., Nair, R. R. & Geim, A. K., 'Manifestation of ripples in free-standing graphene in lattice images obtained in an aberration-corrected scanning transmission electron microscope', *phys. stat. sol. A* 206 (6), 1117-1122 (2009a)

Bangert, U., Gass, M. H., Bleloch, A. L., Nair, R. R. & Eccles, J., 'Nanotopography of graphene' *phys. stat. sol. A,* 206 (9), 2115-2119 (2009b)

Bangert, U., Bleloch, A. L., Gass, M. H., Seepujak, A. & Vandenberg, J., 'Doping of few-layered graphene and carbon nanotubes using ion implantation', *Phys. Rev. B* 81(24), 245423 (2010a)

Bangert, U., Pan, C.-T., Nair, R. R. & Gass, M. H., 'Atomic structure and low electron loss characteristics of hydrogen-dosed graphene deduced from STEM experiments and DFT-WIEN calculations', *Appl. Phys. Lett.*, 97, 253118 (2010b)

Batson, P. E., 'Simultaneous STEM imaging and electron-energy-loss-spectroscopy with atomic-column sensitivity' *Nature* 366 (6457), 727-728 (1993)

Blaha, P., Schwarz,K., Madson, G., Kvasnicka D. & Luitz, J, *User's guide WIEN 2k_10.1* at www.wien2k.at/reg_user/textbooks/usersguide.pdf

Booth, T. J., Blake P., Nair, R. R., Jiang, D., Hill, E.W. , Bangert, U., Bleloch, A. L., Gass, M., Novoselov, K. S. M., Katsnelson , I. & Geim , A. K., 'Macroscopic graphene membranes and their extraordinary stiffness', *Nano Lett.*, 9 (4), 1433-1441 (2008)

Borglund, N., Astrand, P.-G. & Csillag, S., 'Improved background removal method using principal components analysis for spatially resolved electron energy loss spectroscopy' *Microsc. Microanal.* 11(1), 88-96 (2005)

Browning, N. & Pennycook, S., 'Atomic-resolution electron energy-loss spectroscopy in the scanning transmission electron microscope', *J. Microsc.-Oxford* 180, 230-237 (1995)

Brydson, R., *Electron Energy Loss Spectroscopy*, Garland Science, England (2003)

Boukhvalov, D.W. & Katsnelson, M.I., 'Destruction of graphene by metal adatoms', *Appl. Phys. Lett.* 95 (2), 023109 (2009)

Bourelle, E., Konno, H. & Inagaki, M., 'Structural defects created on natural graphite surface by slight treatment of oxygen plasma - STM observations', *Carbon* 37 (12), 2041-2048 (1999)

Chan, K. T., Neaton, J. B. & Cohen, N. L., 'First-principles study of metal adatom adsorption on graphene', *Phys Rev B* 77 (23), 235430 (2008)

Charlier, J.-C., 'Defects in carbon nanotubes', *Acc. Chem. Res.* 35 (12), 1063-1069 (2002)

Charlier, J.-C., Arnaud, L. , Delgado, M., Demoisson, F., Espinosa, E. H., Ewels, C. P., Felten, A., Guillot, J., Ionescu, R., Leghrib, R., Llobet, EMansour, A., Migeon, H-N, Pireaux, J-J., Reniers, F., Suarez-Martinez, I., Watson, G. E. & Zanolli, Z., 'Carbon nanotubes randomly decorated with gold clusters: from nano(2)hybrid atomic structures to gas sensing prototypes', *Nanotechnology* 20 (37), 375501 (2009)

Crespi, V. H., Cohen, M. L. & Rubio, A., 'In situ band gap engineering of carbon nanotubes', *Phys Rev Lett* 79 (11), 2093-2096 (1997)

Duplock, E. J., Scheffler, M. & Lindan, P. J. D, 'Hallmark of perfect graphene', *Phys Rev Lett* 92 (22), 225502 (2004)

Eberlein, T., Bangert, U., Nair, R. R., Jones, R., Gass, M., Bleloch, A. L., Novoselov, K. S., Geim, A. K. & Briddon, P. R., 'Plasmon spectroscopy of free-standing graphene films', *Phys Rev B* 77, 233406 (2008)

Egerton, R. F., *Electron Energy Loss Spectroscopy in the Electron Microscope'*, Plenum Press N.Y. (1986)

Elias, D. C., Nair, R. R., Mohiuddin, T. M. G., Morozov, S. V., Blake, P.,. Halsall, M. P., Ferrari, A. C., Boukhvalov, D. W., Katsnelson, M. I.,Geim, A. K. & Novoselov, K. S., 'Control of Graphene's Properties by Reversible Hydrogenation: Evidence for Graphane', *Science* 323 (5914), 610-613 (2009)

Ewels, C. P., Heggie, M. I. & Briddon, P. R., 'Adatoms and nanoengineering of carbon', *Chem. Phys. Lett.* 351, 178 (2002)

Fall, C. J., Blumenau, A. T., Jones, R., Briddon, P. R., Frauenheim, T.,Gutiérrez-Sosa, A., Bangert, U., Mora, A. E., Steeds, J. W. & Butler, P. E., 'Dislocations in diamond: Electron energy-loss spectroscopy', *Phys. Rev. B* 65 (24), 205206 (2002)

Fasolino, A., Los, J. H. & Katnelson, M. I., 'Intrinsic ripples in graphene', *Nature Materials 6* (11), 858-861 (2007)

Fuentes, G. G., Borowiak-Palen, E., Pichler, T., Liu, X., Graff, A., Behr, G., Kalenczuk, R. J., Knupfer, M. & Fink, J., 'Electronic structure of multiwall boron nitride nanotubes', *Phys. Rev. B* 67 (3), 035429 (2003)

Gan, Y., Sun, L.T, & Banhart F., 'One- and two-dimensional diffusion of metal atoms in graphene', *Small* 4 (5), 587–591 (2008)

Gass, M. H., Bangert, U., Bleloch, A. L., Wang, P., Nair R. R. & Geim, A. K., 'Free-standing graphene at atomic resolution', *Nature Nanotechnology* 3 (11), 676-681, (2008)

Goodhew, P. & Bleloch, A. L., 'SuperSTEM - the microscope with glasses', Mater. World 11 (3), 23-24 (2003)

Haberer, D., Vyalikh, D. V., Taioli, S., Dora, B., Farjam, M., Fink, J., Marchenko, D., Pichler, T., Ziegler, K., Simonucci, S., Dresselhaus, M. S., Knupfer, M., Büchner B.& Grüneis, A., 'Tunable Band Gap in Hydrogenated Quasi-Free-standing Graphene', *Nano Lett.* 10, 3360-3366 (2010)

Hahn, R. & Kang, H., 'Vacancy and interstitial defects at graphite surfaces: Scanning tunneling microscopic study of the structure, electronic property, and yield for ion-induced defect creation', *Phys. Rev. B* 60 (8), 6007-6017 (1999)

HREM Research Inc., DeConvHAADF User's Guide (2009)

Hunt, A. & Williams, D. B., 'Electron energy-loss spectrum imaging', Ultramicroscopy 38 (1), 47-73 (1991)

Ito, A., Nakamura, H. & Takayama, A., 'Molecular Dynamics Simulation of the Chemical Interaction between Hydrogen Atom and Graphene', *J. Phys. Soc. Jpn* 77 (11), 114602 (2008)

Jenkins, G. M., 'Basal plane distortion in pyrolytic carbon', *Carbon* 7, 9 (1969)

Jeanguillaume, C. & Colliex, C., 'Spectrum image- the next step in EELS digital acquisition and processing', *Ultramicroscopy* 28 (1-4), 252-257 (1989)

Leenaerts, O., Partoens, B., Peeters, F. M., 'Adsorption of H_2O, NH_3, CO, NO_2, and NO on graphene: A first-principles study', *Phys. Rev. B* 77 (12), 125416 (2008)

Leenaerts, O., Partoens, B., Peeters, F. M., 'Adsorption of small molecules on graphene', *Microelectronics Journal* 40 (4-5), 860–862 (2009)

Jeloaica, L. & Sidis, V., *Chem. Phys. Lett.* 300, 157 (1999)

Jones, R., Coomer, B. J., Goss, J. P., Hourahine, B. & Resende A., 'The interaction of hydrogen with deep level defects in silicon' in: *Special defects in semiconducting materials,* Volume 71 of *Solid State Phenomena*, Chapter 173-248. Scitech Publications Ltd., Zuerich-Uetikon, Switzerland, (2000)

Kirkland, E., *Advanced Computing in Electron Microscopy*, New York: Plenum (2005)

Kociak, M., Stéphan, O., Henrard, L., Charbois, V., Rothschild, A., Tenne, R. & Colliex, C., 'Experimental evidence of surface-plasmon coupling in anisotropic hollow nanoparticles', *Phys. Rev. Lett.* 87 (7), 077501 (2001)

Krasheninnikov, A. V., Nordlung, K., Sirviö, M., Salonen, E. & Keinonen, J., 'Formation of ion-irradiation-induced atomic-scale defects on walls of carbon nanotubes', *Phys Rev B* 63 (24), 245405 (2001)

Krasheninnikov, A. V., Lehtinen, P. O., Foster, A. S., Pyykko, P., Nieminen, R. M., 'Embedding transition-metal atoms in graphene: structure, bonding, and magnetism', *Phys. Rev. Lett.* 2 (12), 126807 (2009)

Laitenberger, P. & Palmer, R. B., 'Plasmon dispersion and damping at the surface of a semimetal', *Phys. Rev.Lett.* 76 (11), 1952-1955 (1996)

Mao, Y., Juan, J. & Zhong, J., 'Density functional calculation of transition metal adatom adsorption on graphene', *J Phys: Condens Matter* 20 (11), 115209 (2008)

Meyer, J. C., Geim, A. K., Katsnelson, M. I., Novoselov, K. S., Booth, T. J. & Roth, 'The structure of suspended graphene sheets,' *Nature* 446, 60-63 (2007a)

Meyer. J. C., Geim, A. K., Katsnelson, M. I., Novoselov, Obergfell, D., Roth, S., Girit, C. & Zettl, A., 'On the roughness of single- and bi-layer graphene membranes', *Solid State Commun.* 143, 101-109 (2007b)

Meyer, J. C., Kisielowski, C., Erni, R., Rossell, M. D., Crommie, M F & Zettl, A., 'Direct imaging of lattice atoms ond topological defects in graphene membranes' *Nano Lett.* 8(11), 3582 (2008a)

Meyer, J. C., Girit, C. O., Crommie, M. F. & Zettl, A., 'Imaging and dynamics of light molecules on graphene', *Nature* 454, 319-322 (2008b)

Murrell, J. N.& Schmidt, W., *J.* 'Photoelectron spectroscopic correlation of molecular-orbitals of methane, ethane, propane, isobutane and neopentane', *Chem. Soc.-Faraday Trans.II,* 68 (10) 1709-1718 (1972)

Nelhiebel, M., Louf, P. H., Schattschneider, P, Blaha, P, Schwarz, K.& Jouffrey, B., 'Theory of orientation-sensitive near-edge fine-structure core-level spectroscopy', *Phys. Rev. B* 59 (20), 12807-12814 (1999)

Nelson, N. D., Piran T. & S. Weinberg, (eds.) *Statistical Mechanics of Membranes and Surfaces* , World Scientific, Singapore, (2004).

Nordlund, K., Keinonen, J. & Mattila, T., 'Formation of ion irradiation induced small-scale defects on graphite surfaces', *Phys. Rev. Lett.* 77 (4), 699-702 (1996)

Otto, A., 'Theory of plasmon excitations in thin films by electrons of non-normal incidence', *phys. stat. sol.* 22 (2), 401-406 (1967)

Pennycook, S., & Boatner, L.A., 'Chemically sensitive structure-imaging with a scanning transmission electron microscope', *Nature* 336 (6199), 565-567 (1988)

Perez, R. & Que, W., 'Plasmons in isolated single-walled carbon nanotubes', *J. Phys: Condens. Matter* 18 (12), 3197-3216 (2006)

Pomoell, J., Krasheninnikov, A. V., Nordlund, K. & Keinonen, J., 'Stopping of energetic ions in carbon nanotubes', *Nucl. Instr. Meth. in Phys. Res. B* 206, 18-21 (2003).

Raether, H.,' Surface plasma oscillations and their applications' in: *Physics of Thin Films*. Vol 9, p 145ff, Academic Press, New York - London (1977)

Sevincli, H., Topsakal, M., Durgun, E. & Ciraci, S., 'Electronic and magnetic properties of 3d transition-metal atom adsorbed graphene and graphene nanoribbons *Phys Rev B* 77 (19), 195434 (2008)

Sofo, J. O., Chaudhari, A. S. & Barber, G. D., ,Graphane: A two-dimensional hydrocarbon', *Phys. Rev.* B 75 (15), 153401 (2007)

Stéphan, O., Taverna, D., Kociak, M., Suenaga, K., Henrard, L. & Colliex, C., 'Dielectric response of isolated carbon nanotubes investigated by spatially resolved electron energy-loss spectroscopy: From multiwalled to single-walled nanotubes', *Phys. Rev. B* 66 (15), 155422 (2002)

Stolyarova, E., Rim, K.- T., Ryu, S. M., Maultzsch, J., Kim, P., Brus, L. E., Heinz, T. F., Hybertsen, M. S. & Flynn, G. W., 'High-resolution scanning tunneling microscopy imaging of mesoscopic graphene sheets on an insulating surface', Proceedings of PNAS of the U. S. A, 104 (22), 9209-9212, May 2007

Suarez-Martinez, I., Felten, A., Pireaux, J. J., Bittencourt, C. & Ewels, C. P., 'Transition Metal Deposition on Graphene and Carbon Nanotubes' *J Nanosci. Nanotechnol*. 9 (10), 6171-6175 (2009)

Telling, R. H. & Heggie, M. I., 'Radiation defects in graphite', *Phil Mag* 87 (31), 4797-4846 (2007)

Terrones, M. & Terrones, H., 'The role of defects in graphitic structures', *Fullerene Sci and Tecnol* 4 (3), 517-533 (1996)

Uchoa, B., Lin, C.-Y. & Neto, A. H. C, 'Tailoring graphene with metals on top' *Phys Rev B* 77 (3), 35420 (2008)

Varns, R. & Strange, P., 'Stability of gold atoms and dimers adsorbed on graphene', *J. Phys.: Condens. Matter* 20 (22), 225005 (2008)

Xue, K. & Xu, Z.-P., 'Strain effects on basal-plane hydrogenation of graphene: A first-principles study', *Appl. Phys. Lett.* 96 (6), 063103 (2010)

Zhou, Z.-H., Gao, F. & Goodman, D. W., 'Deposition of metal clusters on single-layer graphene/Ru (0001): Factors that govern cluster growth', *Surface Science* 604 (13-14), L31–L38 (2010)

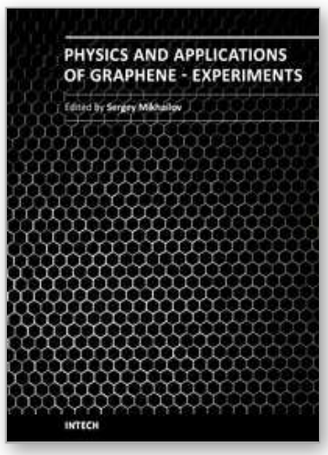

Physics and Applications of Graphene - Experiments

Edited by Dr. Sergey Mikhailov

ISBN 978-953-307-217-3
Hard cover, 540 pages
Publisher InTech
Published online 19, April, 2011
Published in print edition April, 2011

The Stone Age, the Bronze Age, the Iron Age... Every global epoch in the history of the mankind is characterized by materials used in it. In 2004 a new era in material science was opened: the era of graphene or, more generally, of two-dimensional materials. Graphene is the strongest and the most stretchable known material, it has the record thermal conductivity and the very high mobility of charge carriers. It demonstrates many interesting fundamental physical effects and promises a lot of applications, among which are conductive ink, terahertz transistors, ultrafast photodetectors and bendable touch screens. In 2010 Andre Geim and Konstantin Novoselov were awarded the Nobel Prize in Physics "for groundbreaking experiments regarding the two-dimensional material graphene". The two volumes Physics and Applications of Graphene - Experiments and Physics and Applications of Graphene - Theory contain a collection of research articles reporting on different aspects of experimental and theoretical studies of this new material.

InTech Europe
University Campus STeP Ri
Slavka Krautzeka 83/A
51000 Rijeka, Croatia
Phone: +385 (51) 770 447
Fax: +385 (51) 686 166
www.intechopen.com

InTech China
Unit 405, Office Block, Hotel Equatorial Shanghai
No.65, Yan An Road (West), Shanghai, 200040, China
中国上海市延安西路65号上海国际贵都大饭店办公楼405单元
Phone: +86-21-62489820
Fax: +86-21-62489821

IntechOpen